ADVANCED FUNCTIONAL MATERIALS
www.afm-journal.de

PbSe Quantum Dot Superlattice Thin Films for Thermoelectric Applications

Viviana Sousa, Masahiro Goto, Marcel S. Claro, Sergey Pyrlin, Luis Marques, Evgeny B. Modin, Oleg I. Lebedev, Siavash M. Alizadeh, Cátia Freitas, Eliana M. F. Vieira, Kirill Kovnir, Pedro Alpuim, Takao Mori, and Yury V. Kolen'ko**

An unusual self-assembly pattern is observed for highly ordered 1500-nm-thick films of monodisperse 13-nm-sized colloidal PbSe quantum dots, originating from their faceted truncated cube-like shape. Specifically, self-assembled PbSe dots exhibited attachment to the substrate by <001> planes followed by an interconnection through the {001} facets in plan-view and {110}/{111} facets in cross-sectional-view, thus forming a cubic superlattice. The thermoelectric properties of the PbSe superlattice thin films are investigated by means of frequency domain thermoreflectance, scanning thermal probe microscopy, and four-probe measurements, and augmented by computational efforts. Thermal conductivity of the superlattice films is measured as low as 0.7 W m^{-1} K^{-1} at room temperature due to the developed nanostructure. The low values of electrical conductivity are attributed to the presence of insulating oleate capping ligands at the dots' surface and the small contact area between the PbSe dots within the superlattice. Experimental efforts aiming at the removal of the oleate ligands are conducted by annealing or molten-salt treatment, and in the latter case, yielded a promising improvement by two orders of magnitude in thermoelectric performance. The result indicates that the straightforward molten-salt treatment is an interesting approach to derive thermoelectric dot superlattice thin films over a centimeter-sized area.

1. Introduction

The research related to semiconducting quantum dots is an essential subject of nanoscience[1] that recently has culminated in the 2023 Nobel Prize in Chemistry.[2] Colloidal quantum dots (CQDs) are synthesized by methods that employ long-chain organic capping ligands (e.g., oleate, alkylamine, trioctylphosphine) to passivate the surface of quantum dots and to provide a barrier to coalescence, and hence, the resultant CQDs form stable colloidal dispersions in nonpolar organic solvents.[3] Interestingly, monodisperse CQDs could be used as building blocks for bottom-up assembly of nanocrystal superlattices-artificial solids wherein the dots take the place of atoms in traditional solids and the packing arrangement of the dots determines the unit cell parameters of the resultant superstructure.[4] Colloidal dispersion of the dots can generate self-organized thin films through slow evaporation of the solvent, thus

V. Sousa, S. Pyrlin, L. Marques, P. Alpuim
Center of Physics of the Universities of Minho and Porto
University of Minho
Braga 4710-057, Portugal

V. Sousa, S. M. Alizadeh, C. Freitas, P. Alpuim, Y. V. Kolen'ko
International Iberian Nanotechnology Laboratory
Braga 4715-330, Portugal
E-mail: yury.kolenko@inl.int

M. Goto, T. Mori
National Institute for Materials Science (NIMS)
Research Center for Materials Nanoarchitectonics (MANA)
1-1 Namiki, Tsukuba 305-0044, Japan
E-mail: MORI.Takao@nims.go.jp

M. S. Claro
CiQUS, Centro Singular de Investigacion en Quimica Bioloxica e Materiais Moleculares
Departamento de Quimica-Fisica
Universidade de Santiago de Compostela
Santiago de Compostela 15782, Spain

The ORCID identification number(s) for the author(s) of this article can be found under https://doi.org/10.1002/adfm.202409216

DOI: 10.1002/adfm.202409216

S. Pyrlin, L. Marques
Laboratory of Physics for Materials and Emergent Technologies
Lap MET
University of Minho
Braga 4710-057, Portugal

E. B. Modin
CIC nanoGUNE
Donostia, San Sebastian 20018, Spain

O. I. Lebedev
Laboratoire CRISMAT
UMR 6508, CNRS-ENSICAEN
Caen 14050, France

E. M. F. Vieira
CMEMS-UMinho
University of Minho
Guimarães 4800-058, Portugal

E. M. F. Vieira
LABBELS-Associate Laboratory
Braga/Guimarães Portugal

K. Kovnir
Department of Chemistry
Iowa State University
Ames, IA 50011, USA

affording scalable fabrication of highly ordered quantum dot solids.[5] During the late stage of solvent evaporation, the concentration of CQDs increases, and the capillary forces become effective, enabling the self-assembly of the concentrated dispersion of the dots into solid close-packed thin film.[4,6] The as-derived self-assembled highly ordered superstructures have demonstrated properties different from those of a collection of individual dots or other structural building blocks. Such synergistic effects are promising for materials design in energy conversion/storage and nanoelectronics applications.[6–9] The properties can include increased charge transport, delocalization of charge carriers, and unique optoelectronic properties.[10] For instance, self-assembled close-packed arrangements with oriented/exposed facets can improve the selectivity and activity of the catalysts, improving their overall performance and stability.[6] Also, well-organized mesostructures have shown optimized mass diffusion and tunable micro-electric fields, leading to enhanced performance in energy storage and electrocatalysis applications.[9]

CQDs hold promise in solution-processed thermoelectrics (TEs),[11] wherein CQDs with TE properties could be used as building blocks for the fabrication of either highly-ordered or randomly-ordered TE thin films, as well as bulky solids.[12,13] The TE performance of the material is defined by the figure-of-merit $ZT = S^2 \sigma T/\kappa$ (S = Seebeck coefficient; σ = electrical conductivity; T = absolute temperature; κ = thermal conductivity), hence, high S and σ, as well as low κ are beneficial for high-performing TEs.[14] The small size of the dots, below the Bohr radius of an exciton, leads to the quantum confinement effect.[3,12] This phenomenon results in the alterations of the electronic density-of-states near the Fermi energy forming sharp features. Such perturbations could increase charge carrier concentration and mobility, thus effectively enhancing S.[3,15–17] Wang and co-workers demonstrated the increased S for PbSe superlattices due to the strong quantum confinement of the dots with size below 10 nm.[18] On the other hand, the small dimension of the CQDs provides improved phonon scattering at the interfaces between the dots, thus affording lower κ.[19,20] Such thermoelectric thin films are expected to be utilized in IoT energy harvesting applications,[21] leading to the demonstration of several thin film thermoelectric power generation devices.[22–24] Notably, besides exhibiting interesting thermoelectric properties, PbSe consists of more abundant elements (e.g., in comparison with Bi or Te) and can be easily synthesized in the form of CQDs with uniform size and morphology for self-assembling of superlattices.[25–30] In turn, PbSe CQD superlattices can unveil potential for thermoelectric applications near room temperature due to improved performance from ordered-nanoscale, while currently this material is applied to medium-high range temperatures.[3]

When considering σ of solid CQD ensembles, one could expect enhanced σ in superlattices as a consequence of the delocalization of the charge transport,[11] which boosts charge carrier mobility and diffusion length in highly ordered CQD arrays.[19,28] In many cases, high σ was proved difficult to achieve for CQD superlattices. There are two main reasons for this: i) the presence of passivating long-chain insulating organic capping ligand (e.g., oleate) on the surface of CDQs,[31] and ii) the small contact conductance between typically spherical CQDs.[32] In terms of electronic interparticle interactions, short and noninsulating capping ligands are preferred for maximizing charge transfer (both dot–dot and dot–medium); alternatively, insulating capping ligands could be removed by heat treatment or ligand stripping approaches.[33–35] For example, Talapin and Murray reduced interparticle space and improved the electrical conductance of the CQD ensemble from 10^{-11} to 3×10^{-10} S cm^{-1} through the removal of a part of insulating oleate ligands from the surface of PbSe dots. Additional post-treatment with hydrazine solution in acetonitrile allowed for further improved conductance by ten orders of magnitude.[36] In another example, Abelson et al. replaced oleate ligands with 1,2-ethylenediamine enabling the fusion of PbSe CQDs, and then additionally removed long insulating surface ligands by dipping the resultant PbSe superlattice thin film into a PbI_2 solution. Such dual treatment allowed for improved charge carrier mobility. The authors also addressed the problem of the small contact conductance between the dots by atomic layer deposition of alumina, which filled the voids in the superlattice, thus further improving charge carrier mobility, from ≈1 cm^2 V^{-1} s^{-1} to more than 2 cm^2 V^{-1} s^{-1}.[27] Another interesting approach to reduce interparticle space and improve the electronic transport of CQD superlattices relies on the removal of insulating organic capping ligands with the help of molten salts.[37,38] The salts have been applied as electrolytes due to their high ionic conductivity and high electrochemical/thermal stability, in particular, halide molten salts, such as iodine-, chloride-, and fluoride-based.[39] Notably, iodine-based molten salts are in the lowest temperature range, i.e., below the temperature of CQDs' sintering, and hence, could be employed to improve the electronic performance of semiconductor CQD thin films.

In this paper, we report the results of our computational investigation of PbSe CQD thin films followed by an experimental study of the fabrication and properties evaluation of PbSe CQD superlattice thin films. A series of pristine, annealed, molten-salt-treated superlattice thin films with similar structures has been studied where the thermal and electrical transport properties differ depending upon fine ordering and real microstructure. The substantial improvement of the thermoelectric performance of molten-salt-treated PbSe superlattice thin films has been experimentally demonstrated.

2. Result

2.1. Theoretical Insights on Electronic Transport of PbSe CQD Thin Films

To understand the potential of PbSe CQD superlattice thin films as thermoelectric materials, an analysis of the electronic transport coefficients based on ab initio calculations was performed. The calculations have been conducted for several envisioned cases, namely, for the reference bulk PbSe, the reference nanostructured bulk PbSe, highly-ordered self-assembly of PbSe dots (i.e., superlattice), and randomly-ordered self-assembly of PbSe dots (i.e., nonsuperlattice). Moreover, the calculations anticipate

K. Kovnir
U.S. Department of Energy
Ames National Laboratory
Ames, IA 50011, USA

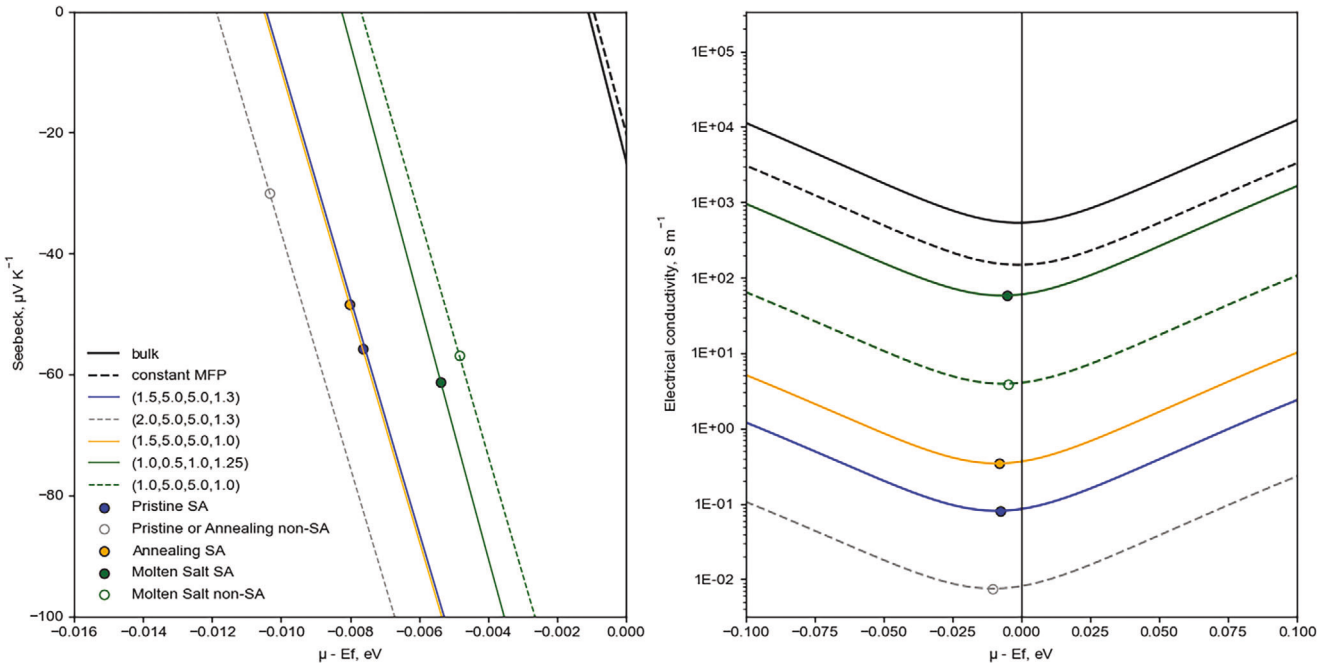

Figure 1. Calculated profiles of Seebeck coefficient (left) and electric conductivity (right) as the function of chemical potential for the selected set of parameters. For the fitted profiles the set of figures in the legend shows the chosen values of the corresponding parameter: w_{GB} (nm), U_{GB} (eV), U_{pore} (eV), and R_{pore}/R_0. Circle markers indicate the points on the profile, closest to the experimental measurements presented below. Filled circles and solid color lines correspond to superlattice (SA) CQD arrays, while open circles and dashed grey and green lines to nonsuperlattice (non-SA) CQD arrays. The black solid line indicates the reference transport coefficients of a bulk PbSe. The dashed black line demonstrates the attempt to model the effect of nanostructuring using a constant mean free path (MFP) approximation.

the case of pristine ensembles of PbSe dots having oleate capping ligands, as well as the cases of ensembles of PbSe dots wherein oleate capping ligands have been partially removed by annealing or molten-salt heat-treatment. Based on the previously published studies of similar CQDs, oleate capping ligands form a rather large shell (1.1–2.1 nm in thickness) around the dots.[18,27,36] To account for this, the model included scattering of charge carriers by periodic rectangular potential barriers, representing interdot contacts. The width of such "grain boundary" potentials, w_{GB}, was expected to be in 0.5–2.5 nm range. Regarding the height of the potential barriers, in several studies, the contact barrier energy of the order ≈0.1 eV was suggested.[40,41] At the same time, tunneling over a large pore should be similar to the work functions of typical conductors, so the upper value for interdot contact barriers, U_{GB}, as well as for spherical barriers, representing pores in dot superlattice, U_{pore}, was limited to 5 eV. For convenience, the values of potential barriers and band energies are given with respect to the Fermi energy, E_F, of PbSe. Additional exploration of the influence of U_{GB}, U_{pore}, and normalized pore radius, R_{pore}/R_0, on electronic transport within PbSe CQD ensembles are presented in Figures S1–S5 (Supporting Information).

The calculated profiles of the Seebeck coefficient, $S(\mu)$, and electrical conductivity, $\sigma(\mu)$, are shown in **Figure 1** and Figure S6 (Supporting Information). Depending on the degree of nanostructuring, the electrical conductivity reduces from 10^3 to 10^4 S m^{-1}, typical for bulk PbSe,[42–45] down to 10^{-9} S m^{-1} for pristine PbSe CQD thin film with large oleate shell.[36] At the same time, the Seebeck coefficient experiences relatively small dispersion with nanostructuring. In fact, the most prominent change for $S(\mu)$ from its bulk profile is a displacement toward negative values of $(\mu–E_F)$. This displacement is a result of band filtering by boundary scattering: while PbSe dots themselves appear to be slightly doped in favor of holes, for the whole superlattice, the electrons of conduction bands have higher mobility as they are more likely to tunnel through interdot barriers. This effect is not reproduced either by constant relaxation time or by constant mean free path (MFP) approximations, highlighting the importance of detailed modeling of scattering times.

Regarding electrical conductivity, our experimental data for the PbSe CQD film treated with molten salts evidenced almost complete ligand removal and substantial electrical conductivity increase (vide infra). To mimic a nearly complete ligand removal procedure, we lower the interdot distance, w_{GB}, down to 1 nm, i.e., almost down to direct contact. For pristine (no ligand removal) and annealed (partial ligand removal) samples the values of w_{GB} in the range of 1.5–2.0 nm were found appropriate, and set U_{GB} and U_{pore} down to 0.5 and 1.0 eV, respectively, while the maximum setting of 5.0 eV worked well for the rest of the film specimens. The computational results suggest that molten salt treatment seems to effectively eliminate oleate ligands leading to the fusion of the PbSe dots within the ensemble, thus establishing interfaces with lower barriers and higher area.

The concentration of free carriers of each type (n, p), as well as corresponding scattering times, $\langle\tau_{e,h}\rangle$, and mobilities, $\langle\mu_{e,h}\rangle$, were also estimated (**Table 1**). While the estimated concentration of free charge carriers is quite similar across three film samples, the mobility of molten-salt-treated PbSe CQD film again stands out,

Table 1. Calculated electronic transport properties of superlattice and nonsuperlattice regions of pristine, annealed, and molten-salt-treated PbSe CQD thin films.

Electronic properties		μ-E_f, eV	Electrons			Holes		
			n_{bulk}, cm^{-3}	$<\tau_e>$, s	$<\mu_e>$, cm^2 V^{-1} s^{-1}	p_{bulk}, cm^{-3}	$<\tau_h>$, s	$<\mu_h>$ cm^2 V^{-1} s^{-1}
Pristine	superlattice	−0.008	9.6×10^{15}	9.6×10^{-16}	6.23	16.0×10^{15}	9.5×10^{-16}	6.19
Pristine or Annealing	nonsuperlattice	−0.010	8.7×10^{15}	9.6×10^{-16}	6.23	17.7×10^{15}	9.5×10^{-16}	6.20
Annealing	superlattice	−0.008	9.5×10^{15}	9.5×10^{-16}	6.18	16.2×10^{15}	9.4×10^{-16}	6.15
Molten salt	superlattice	−0.005	10.5×10^{15}	4.0×10^{-14}	261	14.6×10^{15}	2.6×10^{-14}	168
	nonsuperlattice	−0.005	10.7×10^{15}	1.2×10^{-15}	7.84	14.3×10^{15}	1.0×10^{-15}	6.69

showing a striking imbalance between concentrations of holes and electrons, and their mobilities. A similar behavior is commonly reported for crystalline bulk materials, wherein the mobilities of electrons are often higher than the mobilities of holes. For example, III–V InSb semiconductor demonstrates markedly higher electron mobilities of up to 77 000 cm^2 V^{-1} s^{-1} in comparison to the maximum hole mobilities of ≈850 cm^2 V^{-1} s^{-1}. The estimated concentrations of free carriers n_{bulk} and p_{bulk} were determined by integration of electronic density-of-states calculated for bulk PbSe for the estimated value of chemical potential. Taking into account the excluded volume of pores and interdot distance (or oleate ligand shell if present) $n_{\text{eff}} = 4.4 \pm 0.1 \times 10^{15}$ cm^{-3} and $p_{\text{eff}} = 7.2 \pm 1.2 \times 10^{15}$ cm^{-3} can be estimated for effective concentrations of free carriers in the PbSe CQD superlattice.

2.2. Large Area PbSe CQD Superlattice Thin Films

We further studied promising electrical transport of PbSe CQD superlattices, confirmed from theoretical insights, by performing a detailed structural and properties characterization of PbSe superlattices in the form of thin films. Our previously reported colloidal synthesis method was adapted to prepare monodisperse oleate-capped PbSe CQDs with narrow dot size distribution of 13 ± 1 nm and cubic crystal structure (*Fm*–3*m*, *a* = 6.1256(2) Å, ICDD no. 04-002-6293, Figure S7a, Supporting Information).[16] To obtain a self-assembled thin film from the as-synthesized 13-nm-sized PbSe CQDs, a 10 mg L^{-1} dispersion of the dots in toluene was prepared, and the solvent was evaporated completely over hydrophobized 1 × 1 cm SiO_2/Si wafer or W foil substrates. The solvent evaporation process was managed to be very slow, namely, in a time spun of 20 days. Moreover, the substrates were tilted to 45 ° to increase the contact area during the process of slow evaporation, hence, promoting the reproducible deposition of self-assembled PbSe CQD thin film with a thickness of 1.5 ± 0.6 µm (Figure S8, Supporting Information).

Optical photo (Figure S9, Supporting Information) and scanning electron microscopy (SEM) studies (Figure S10, Supporting Information) show a co-existence of a relatively large brighter area (≈0.33 cm^2) in the middle of the resultant thin films (Figure S9, Supporting Information), corresponding to the highly-ordered self-assembly (i.e., superlattice region) (**Figure 2**; Figure S10, Supporting Information), together with foggy areas (≈0.67 cm^2) on the top and bottom sides of the fabricated thin films (Figure S9, Supporting Information), corresponding to randomly-ordered self-assembly (i.e., nonsuperlattice region), as observed on left side of Figure S10b (Supporting Information). The ordered arrangement of PbSe CQDs within the resultant superlattice region of the as-fabricated thin films was confirmed by SEM, transmission electron microscopy (TEM), electron diffraction (ED), and scanning TEM (STEM) analyses of the film lamellas fabricated by focused ion beam (FIB) milling. Plan-view SEM images (Figure 2) and cross-sectional-view high-angle annular dark-field STEM (HAADF–STEM) images in **Figure 3** and Figure S8 (Supporting Information) reveal the formation of structurally and chemically uniform, highly-ordered cubic PbSe CQDs 3D superlattice. We found that the true shape of the synthesized PbSe CQDs is truncated-cube-like (**Figure 4**a,b; Figure S11, Supporting Information), i.e., cube-like {100} faceted dots with {110} truncated sides and {111} truncated corners. According to the ED analysis (Figure 3a), the PbSe dots exhibit cubic crystal structure (*Fm*–3*m*, *a* = 6.12 Å, ICSD no. 63097), which is in good agreement with the X-ray diffraction (XRD) data (Figure S7a, Supporting Information). Moreover, the PbSe CQDs demonstrate the most prominent growth direction along [001] and, to a lesser extent, along [110] (Figures 3a and 4a,b; Figures S8 and S11, Supporting Information).

The dots were observed to be attached to the substrate surface by <001> planes and interconnected between themselves through the {001} facets in plan-view and {110}/{111} facets in cross-sectional-view (Figures 2 and 3c,d, and 4a,b; Figure S8, Supporting Information). This is most likely due to oleate ligand attachment effect, which is usually stronger over {110}/{111} facets as a result of higher ligands' density on these facets, exhibiting higher surface energy.[46] Such a self-assembly pathway provides access to the nearly perfect cubic ordering of the dots within the superlattice, as confirmed by ED pattern near the central diffraction beam (Figure 3b), which was collected using maximal camera length. From this ED data, the ordering period of the superlattice was estimated to be ≈17 nm, which is in good agreement with the SEM and HAADF–STEM imaging shown in Figures 2 and 3d, respectively.

Notably, the most common self-organization of nearly spherical CQDs deposited onto a sufficiently flat substrate is 2D hexagonal ordering, but in our case, the 13-nm-sized PbSe CQDs are largely arranged to form cubic superlattice, with only a limited appearance of hexagonal ordering. For example, Figure S12 (Supporting Information) shows the occasional co-existence of cubic and hexagonal orderings of the dots, which was found only at the

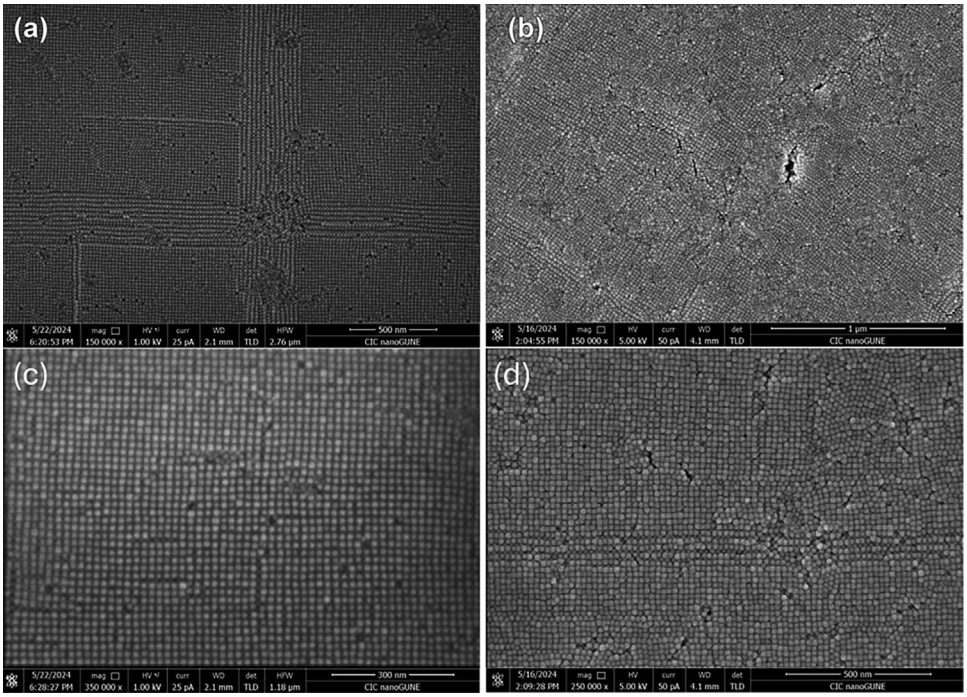

Figure 2. Representative plan-view SEM images at a,b) lower and c,d) higher magnification of a,c) pristine PbSe CQD superlattice thin film, and b,d) after the film being subjected to annealing at 400 °C under vacuum for 15 min plus under H_2 gas flow of 100 mL min^{-1} for 5 min.

edge of the superlattice thin film. The primary ordering of the dots through the superlattice thin film was established to be cubic, as revealed by TEM imaging and the corresponding ED data. The energy dispersive X-ray spectroscopy analysis in STEM mode (STEM–EDX) confirms the expected chemical composition of the PbSe dots (Pb/Se atomic ratio is 1:1), as well as uniform distribution of key constituting elements Pb and Se through the dot building blocks and the whole superlattice thin film (Figure 3e).

To improve the charge transport properties of as-fabricated PbSe CQDs superlattice thin films, two different thermal treatments were applied to the thin films: i) short annealing at 400 °C under vacuum for 15 min followed by annealing under H_2 gas flow of 100 mL min^{-1} for 5 min, and ii) heat treatment in a molten salt mixture of CsI/LiI = 2:1 at 200 °C under Ar gas flow of 100 mL min^{-1} for 30 min. Such treatments are anticipated to partially or completely eliminate the insulating capping oleate ligands around the PbSe dots, and consequently, improve dot interconnection while suppressing their sintering.[6,47] To evaluate the effectiveness of the employed ligand removal protocols, infrared spectroscopy was carried out to analyze the resultant PbSe CQD thin films (Figure S13, Supporting Information). Normally, oleate ligands capping PbSe dots are reported with higher intensities ≈2950, 2900, 2850 cm^{-1}, and ≈1500 cm^{-1}.[27,29,30,48] According to infrared spectroscopy, the presence of some oleate ligands was still observed for the annealed films, but there was almost a complete removal of organic compounds from the molten-salt-treated films, as deduced from the decreased peaks intensities in the Figure S13 (Supporting Information).

According to the XRD analysis, the PbSe CQDs in superlattice thin films preserve their original cubic crystal structure after being subjected to the aforementioned treatments (Figure S7b,c, Supporting Information). Notably, after the heat treatments lattice parameter increased slightly from original $a = 6.1256(2)$ Å to annealed $a = 6.1278(3)$ Å and molten-salt-treated $a = 6.1284(2)$ Å samples, suggesting a small increase in the mean size of the dots (Figure S7, Supporting Information). Additional electron microscopy studies of the treated samples led to the observation that the PbSe CQDs are more closely packed within the annealed thin film (Figures 2d, 3b,d, and 4c; Figure S10b and S14, Supporting Information), which is consistent with the observed partial oleate ligand removal around the dots (Figure S13, Supporting Information). The microstructure of the thin film treated in molten salt (**Figure 5**) is somewhat more similar to the one of the pristine PbSe CQD superlattice (Figures 3; Figure S8, Supporting Information), albeit a small increase in the mean size of PbSe dots was observed, consistent with XRD data above. Importantly, both treatments avoided complete sintering of the dots upon the intended removal of the oleate ligand (Figure 5; Figures S10b,c, and S14, Supporting Information). At the same time, we detected the initial tendency of the PbSe dots to sinter during thermal annealing (Figure 4c,d), while we did not observe any signature of dots' sintering during molten salt treatment (Figure 5). The TEM imaging shows that the superlattice structure becomes less ordered (superlattice domain sizes decrease) after the treatments when compared to one in the pristine superlattice thin film (Figure 3; Figure S8, Supporting Information *cf.* Figure 5; Figure S14, Supporting Information), and as a result more stacking faults can be found within treated thin films (Figure 5; Figure S14, Supporting Information). The STEM–EDX analyses of the lamellas show that the regions containing Pb and Se well overlap with each other (Figure 5; Figure S14, Supporting Information),

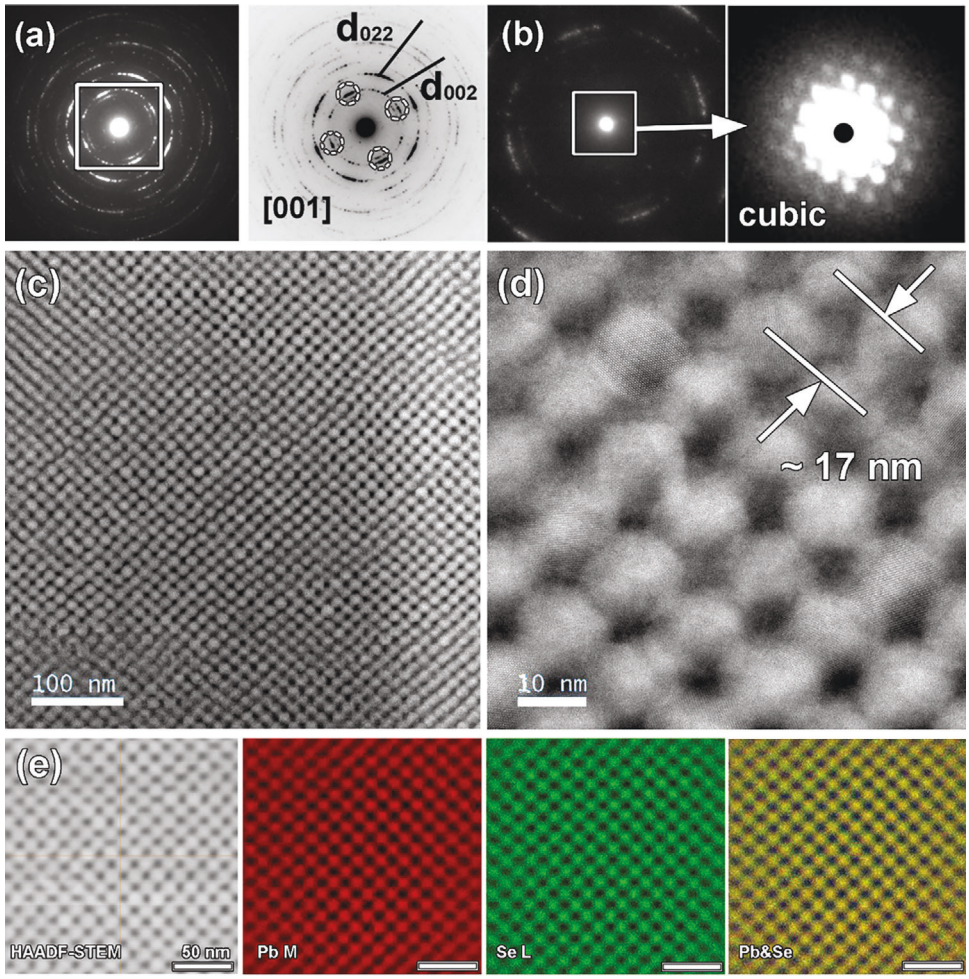

Figure 3. Representative cross-section HAADF–STEM images of CQD film area at different magnifications c,d) and the corresponding ED patterns a,b) of the lamella fabricated by FIB milling of self-assembled PbSe CQD thin film, together with the simultaneously collected e) STEM–EDX maps of Pb, Se, and their superposition.

indicating the homogeneous distribution of the elements within treated superlattice thin films, as well as evidencing the preservation of the chemical composition of the PbSe dots after both applied treatments.

2.3. Low Thermal Conductivity of the PbSe CQD Superlattice Thin Films

The thermal transport properties of three types of PbSe CQD superlattice thin films (i.e., pristine, annealed, and molten-salt-treated) were probed by the frequency domain thermoreflectance (FDTR) which has a good sensitivity for κ in the direction normal to the surface $\kappa_{\perp}$. We found that the FDTR measurements within the same superlattice film deposited onto the SiO_2/Si wafer substrate showed considerable inhomogeneities in reflectivity and phase-shift, which may be attributed to the variations in the film thickness and local film properties, such as superlattice domain size and the degree of dots' ordering. Since $\kappa_{\perp}$ and heat capacity, C_p, extracted from the FDTR phase-shift model are correlated to these local properties, neither the thermal properties nor film properties could be obtained independently for each point. Nevertheless, after measuring over several different points, an average curve for each film specimen was determined. Those average curves were alike for all three measured superlattice thin films, and it was concluded that the average values of $\kappa_{\perp}$ and C_p for all three films are similar within the obtained error margins.

Figure 6 shows the collected FDTR data corresponding to the film thickness of 1.34 µm ± 10%, $\kappa_{\perp} = 0.69$ W m^{-1} K^{-1} ± 30%, and $C_p = 1.14 \times 10^6$ J m^{-3} K^{-1} ± 9%. The calculated heat capacity of ≈0.14 J g^{-1} K^{-1} is close to the previously reported value for bulk PbSe of ≈0.17 J g^{-1} K^{-1}, confirming fitting robustness.[49] Interestingly, the measured room temperature thermal conductivity of the superlattice thin films is 56% lower when compared with $\kappa = 1.6$ W m^{-1} K^{-1} of bulk PbSe.[50] Furthermore, we attempted to perform thermal property mapping employing FDTR. The maps of reflectivity and phase-shift (from where $\kappa_{\perp}$ and C_p were extracted) for three types of thin films were acquired at total reflectivity, as well as at modulation frequencies of 7.25 kHz and 2.76 MHz over 160 × 160 µm^2 superlattice film area. The results of this effort are presented in Figures S15–S17 (Supporting Information), which confirm the similar homogeneity of thermal

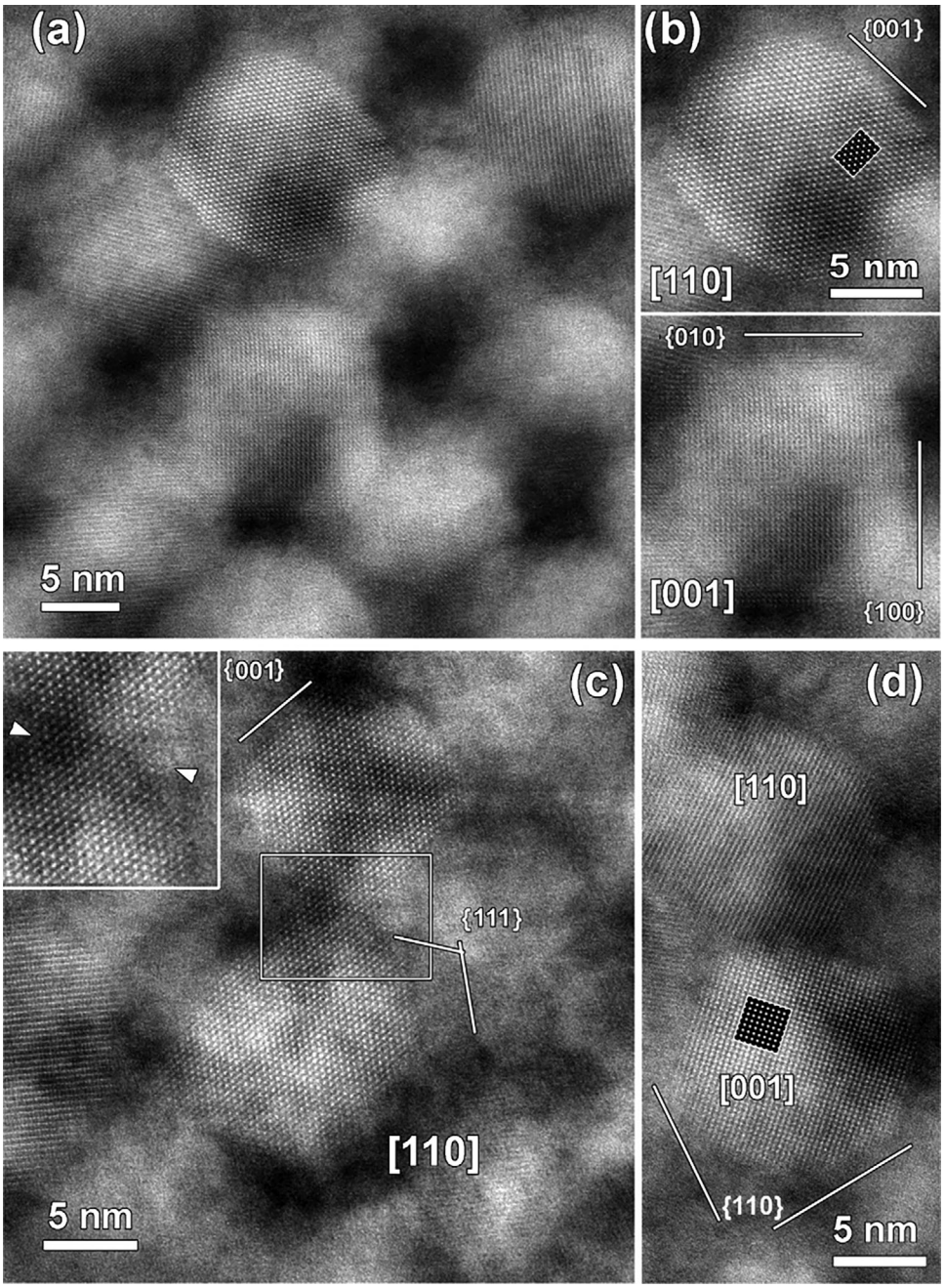

Figure 4. Representative cross-section high-resolution HAADF–STEM images of a) pristine PbSe CQD superlattice thin film, b) selected [110] and [001] PbSe CQD images; c,d) after the film being subjected to annealing at 400 °C under vacuum for 15 min plus under H_2 gas flow of 100 mL min^{-1} for 5 min. The joint interface between two [110] PbSe CQDs is given as insert in (c) and marked by white arrow heads.

transport properties for all superlattice thin films based on PbSe dots.

2.4. Scanning Thermal Probe Microscopy Probing of Superlattice Thin Films

With promising thermal transport results in hand, we next sought to further investigate TE properties of the fabricated superlattice PbSe CQD thin films. We decided to analyze the self-assembled superlattice as well as nonsuperlattice regions of the thin films to elucidate how the level of ordering in dot packing affects the TE properties. For this purpose, scanning thermal probe microscopy (STPM) was applied providing access to thermal conductivity, thermal effusivity, and thermopower maps for the three fabricated PbSe CQD thin films. It is important to note that the STPM measurements were carried out under air. This could result in air and moisture influencing the heat

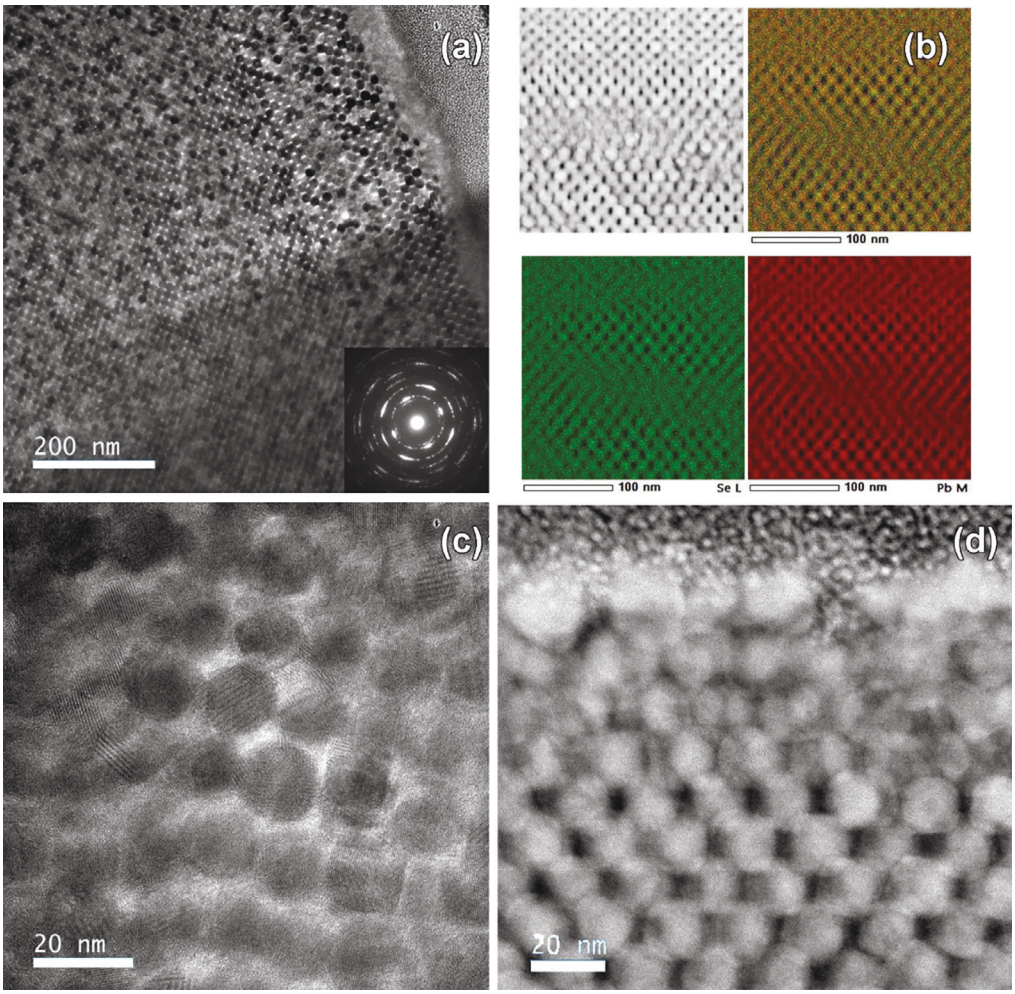

Figure 5. Representative a,c) bright field TEM and d) HAADF–STEM images at different magnifications, and b) low magnification HAADF-STEM image together with corresponding STEM–EDX maps of Pb, Se, and their mixture of the FIB-fabricated lamella of superlattice thin film self-assembled from 13-nm-sized PbSe CQDs, after the film being subjected to the heat treatment in a molten salt mixture of CsI/LiI = 2:1 at 200 °C under Ar gas flow of 100 mL min^{-1} for 30 min.

conduction between the PbSe CQD thin films and the probe, leading to overestimated effusivity and thermal conductivity.[51,52] Therefore, the results obtained from STPM were only considered for relative comparison between pristine, annealed, and molten-salt-treated film specimens, and between superlattice and nonsuperlattice regions of the film specimens. The details of the STPM measurements are presented in Figures S18–S20, (Supporting Information), while Table S1 summarizes the condition of STPM probing. **Table 2** summarizes average values of thermal conductivity, effusivity, and Seebeck coefficient obtained by STPM probing.

Figure 7a,b,c show the respective thermal conductivity maps for STPM-probed areas of 0.49, 0.44, and 0.55 cm^2 for pristine, annealed, and molten-salt-treated film specimens, respectively. Notably, the points with negative values on effusivity and Seebeck measurements, detected during STPM probing, were not considered during the calculation. Also, due to large differences from nearby values, six left columns recorded for the molten-salt-treated thin film were not considered for the average results presented in Table 2. This is most likely due to some defect on the measured area.

Average κ values for the corresponding superlattice/nonsuperlattice regions were estimated to be 13/9.6, 6.9/7.3, and 5.5/3.0 W m^{-1} K^{-1} for pristine, annealed, and molten-salt-treated PbSe CQD thin films, respectively. The data suggests that the thermal treatments of the pristine PbSe CQD thin film targeting oleate ligand removal lead to ≈50% reduction in κ. Comparing κ between superlattice and nonsuperlattice regions, in general, nonsuperlattice regions featuring random ordering were found to be characterized by lower κ than highly ordered superlattice regions, namely, 27% and 45% lower in the case of pristine and molten-salt-treated samples, respectively. However, the annealed sample showed somewhat similar κ for superlattice/nonsuperlattice regions with a difference of ≈5%.

Next, we mapped the thermal effusivity of the fabricated thin films (Figure 7d,e,f), and average values for superlattice/nonsuperlattice regions of the films were

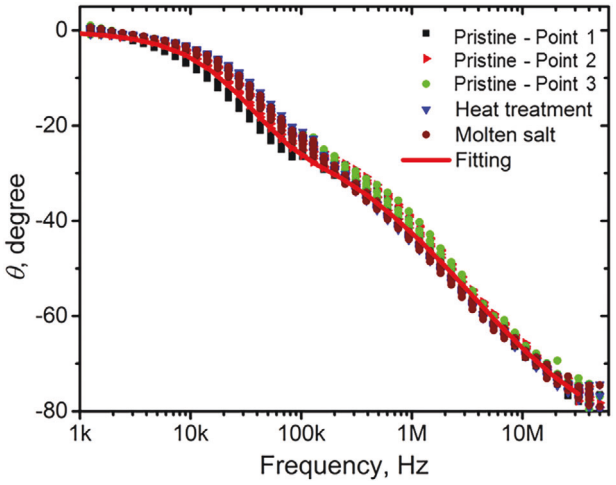

Figure 6. FDTR phase-shift signals of superlattice thin film self-assembled from 13-nm-sized PbSe CQDs recorded at three different points (Pristine – Point 1, Pristine – Point 2, and Pristine – Point 3) of pristine sample, along with average FDTR profiles of the films being subjected to annealing or molten-salt-treatment. The red line shows the best-fitting model.

measured to be $4.2 \times 10^3/3.6 \times 10^3$ J $s^{-0.5}$ m^{-2} K^{-1}, $3.1 \times 10^3/3.2 \times 10^3$ J $s^{-0.5}$ m^{-2} K^{-1}, and $2.7 \times 10^3/2.0 \times 10^3$ J $s^{-0.5}$ m^{-2} K^{-1} in the cases of pristine, annealed, and molten-salt-treated samples, respectively. Thus, effusivity features decrease upon the thermal treatments, as well as in nonsuperlattice regions. Finally, the thermopower was probed (Figures 7g–i). Average Seebeck coefficient values for superlattice/nonsuperlattice regions of the PbSe CQD thin films were established to be −56/−30, −48/−31, and −61/−57 μV K^{-1} for pristine, annealed, and molten-salt-treated samples, respectively. The negative sign of the thermopower demonstrates that the materials are *n*-type with electrons as major charge carriers. The applied thermal treatments moderately impact *S* values.

Finally, we measured the electrical conductivity of PbSe CQD superlattice thin films deposited onto SiO_2/Si wafer substrate by means of the four-probe method. We failed to obtain the electrical conductivity of pristine PbSe superlattice since the values were too low. Nonetheless, we were able to measure the conductivities of annealed and molten-salt-treated PbSe superlattice thin film samples, and the respective values were 0.6 and 58 S m^{-1}. These values are significantly lower than the electrical conductivity of 10^4 S m^{-1} reported for bulk *n*-type PbSe.[50] Nevertheless, molten salt treatment resulted in two orders of magnitude increase in electrical conductivity.

3. Discussion

Self-assembled long-range ordered arrays of CQDs are a powerful strategy for the bottom-up design of hierarchically organized and compositional tunable functional nanomaterials with interesting properties.[53] Self-assembling of the CQDs typically occurs in the form of 2D (thin films) or 3D (micro/meso crystals) arrangements. The assembling process is governed by several features of CQDs, such as size/shape uniformity and nature of capping ligands, as well as by the assembling conditions, such as employed solvents, nonsolvents, substrates, and evaporation rates.[9,54] Depending upon these factors,[5] the resultant ensembles of CQDs could exhibit randomly-ordered closely-packed appearance, highly-ordered superlattice appearance, or coexistence of both disorder/order appearances. In the current study, we found that only the middle area (i.e., ≈33% of the film) of self-assembled 1.5-μm-thick 1 × 1 cm PbSe CQD thin films exhibit highly-ordered superlattice appearance while the nearby regions (i.e., ≈67% of the film) co-existed with randomly-ordered closely-packed appearance (Figure S9, Supporting Information).

Typically, 2D superlattices (i.e., monolayers) from lead chalcogenide CQDs undergo self-assembly into hexagonal structures.[25,53] In contrast to monolayers, PbSe CQD superlattices with more than five layers have been shown to self-assemble preferentially into cubic structures, such as body-centered cubic or face-centered cubic.[25,26] Simple cubic packing is challenging to obtain from spherical dots due to low packing density, while it has been predominantly reported for cubic-shaped dots (**Figure 8b–d**).[55] Pinna and co-workers presented simple-cubic ordering within 40 nm-thick films (i.e., 10 layers of rhombicuboctahedron-shaped PbSe dots) after ligand exchange with ethylenediamine.[25] Other reported lead chalcogenide superlattice orderings include rhombohedral and body-centered-tetragonal ones.[27,29,30,54,56] Xu and co-workers showed a face-centered rhombohedral structure for a 500 nm-thick PbSe CQD film with closed-packed structures after ligand exchange with benzoic acid.[48] Nonetheless, the majority of 3D self-assembled lead chalcogenide CQDs superlattices have a few nanometers in thickness.

Table 2. Average values of thermal conductivity, effusivity, and Seebeck coefficient obtained by STPM probing of superlattice and nonsuperlattice regions of pristine, annealed, and molten-salt-treated PbSe CQD thin films.

Sample		Pristine	Annealing	Molten salt
Parameters				
Thermal conductivity, W m^{-1} K^{-1}	superlattice	13 ± 7	6.9 ± 3.5	5.5 ± 3.0
	nonsuperlattice	9.6 ± 5.1	7.3 ± 3.2	3.0 ± 1.8
Effusivity, J $s^{-0.5}$ m^{-2} K^{-1}	superlattice	$4.2 \times 10^3 \pm 1.4 \times 10^3$	$3.1 \times 10^3 \pm 8.9 \times 10^2$	$2.7 \times 10^3 \pm 9.4 \times 10^2$
	nonsuperlattice	$3.6 \times 10^3 \pm 1.1 \times 10^3$	$3.2 \times 10^3 \pm 8.0 \times 10^2$	$2.0 \times 10^3 \pm 7.3 \times 10^2$
Seebeck coefficient, μV K^{-1}	superlattice	−56 ± 23	−48 ± 20	−61 ± 8.7
	nonsuperlattice	−30 ± 24	−31 ± 19	−57 ± 9.4

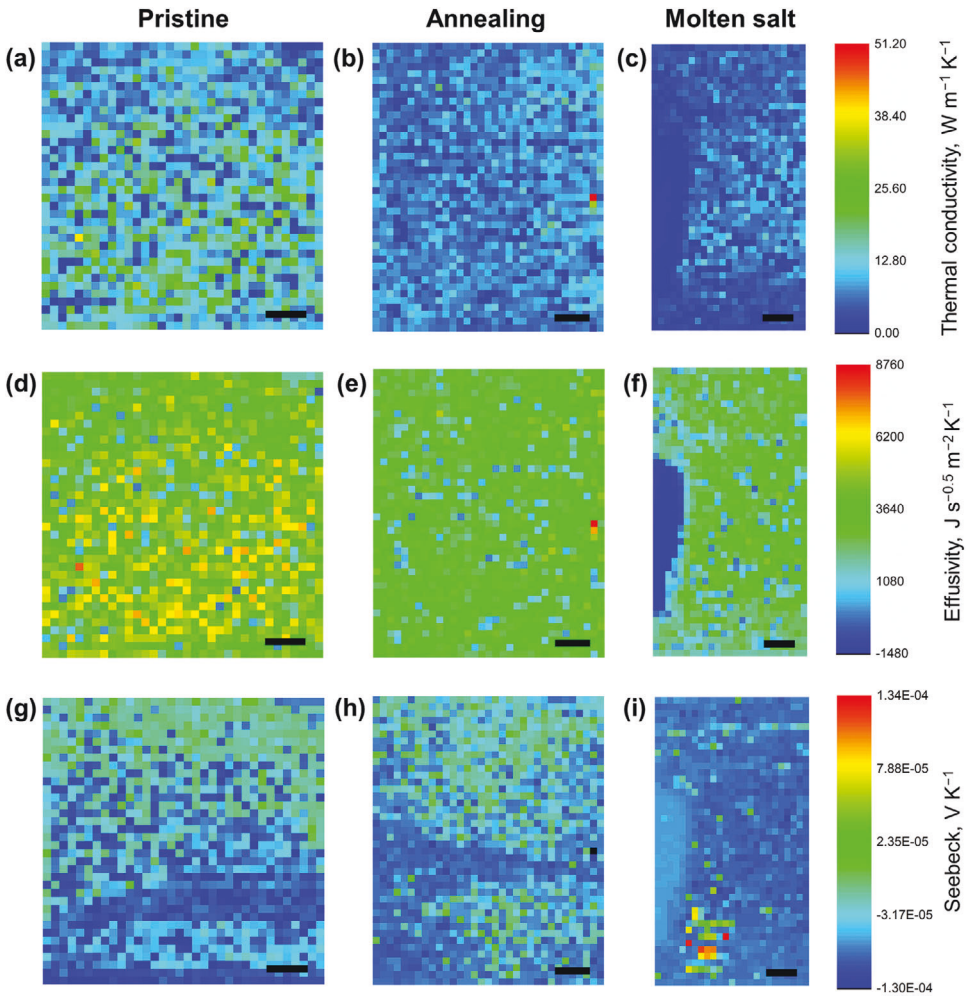

Figure 7. STPM maps of thermal conductivity a–c), thermal effusivity d–f), and thermopower g–i) for pristine a,d,g), annealed b,e,h), and molten-salt-treated c,f,i) PbSe CQD thin films. The black scale bar is equal to 1 mm.

In the present study, we achieved control over the synthesis of truncated-cube-like PbSe CQDs, i.e., cube-like {100} faceted dots with truncated {110} sides and {111} corners (Figure 8a,e–g; Figure S11, Supporting Information). Moreover, the PbSe dots self-assemble among themselves into superlattice in an uncommon fashion via sharing the {110}/{111} facets (Figures 3 and 8h–i; Figures S8 and S21, Supporting Information) while the vast majority of reports in the literature suggest the PbSe dots self-assemble into superlattice through the {100} facets due to lower surface energy of the facets.[46] The observed uncommon self-assembly pathway of our PbSe dots may be related to their size (13 nm) and shape (truncated cubes), which differ from the more commonly used nearly spherical PbSe dots with smaller diameters of 5–7 nm in reported PbSe superlattices.[25–28,59] Notably, oleate ligands exchange/removal has been reported to transform hexagonal superlattices (Figure 8l) into cubic ones due to preferential removal of ligands on {100} facets and their further epitaxial assembling through fusing {100} facets.[27,29,30] In our case, even after partial oleate ligand removal by annealing (Figure 8j; Figures S14, Supporting Information) or after nearly complete oleate ligand removal with help of molten salt treatment (Figures 5 and 8k), the resultant PbSe dots within superlattice thin films retain their attachment to the substrate surface by <001> planes and dots interconnection through the {001} facets in plan-view and {110}/{111} facets in cross-sectional-view (Figure S21, Supporting Information).

Our motivation for the investigation of PbSe CQD superlattice thin films was to probe the effect of ordering and quantum confinement on their TE properties. Such thin films may be potential candidates for fabricating advanced TE devices. In the quantum confinement regime, the semiconductor behavior of CQD is characterized by discrete energy states, which create sharp delta-function-like peaks at the electronic density-of-states (DOS) and alter bandgap energy of the semiconductor material, thus creating minibands.[15,28] For example, Kavrik and co-workers developed epitaxially-fused PbSe CQD superlattices by injection of 1,2-ethylenediamine and ammonium thiocyanate for the formation of 3D and 2D ensembles, respectively, thus obtaining a tunable bandgap from 0.7 to 1.1 eV.[60] Moreover, DOS alteration by quantum confinement usually affords a high Seebeck coefficient and higher charge carrier concentration due to selective carrier

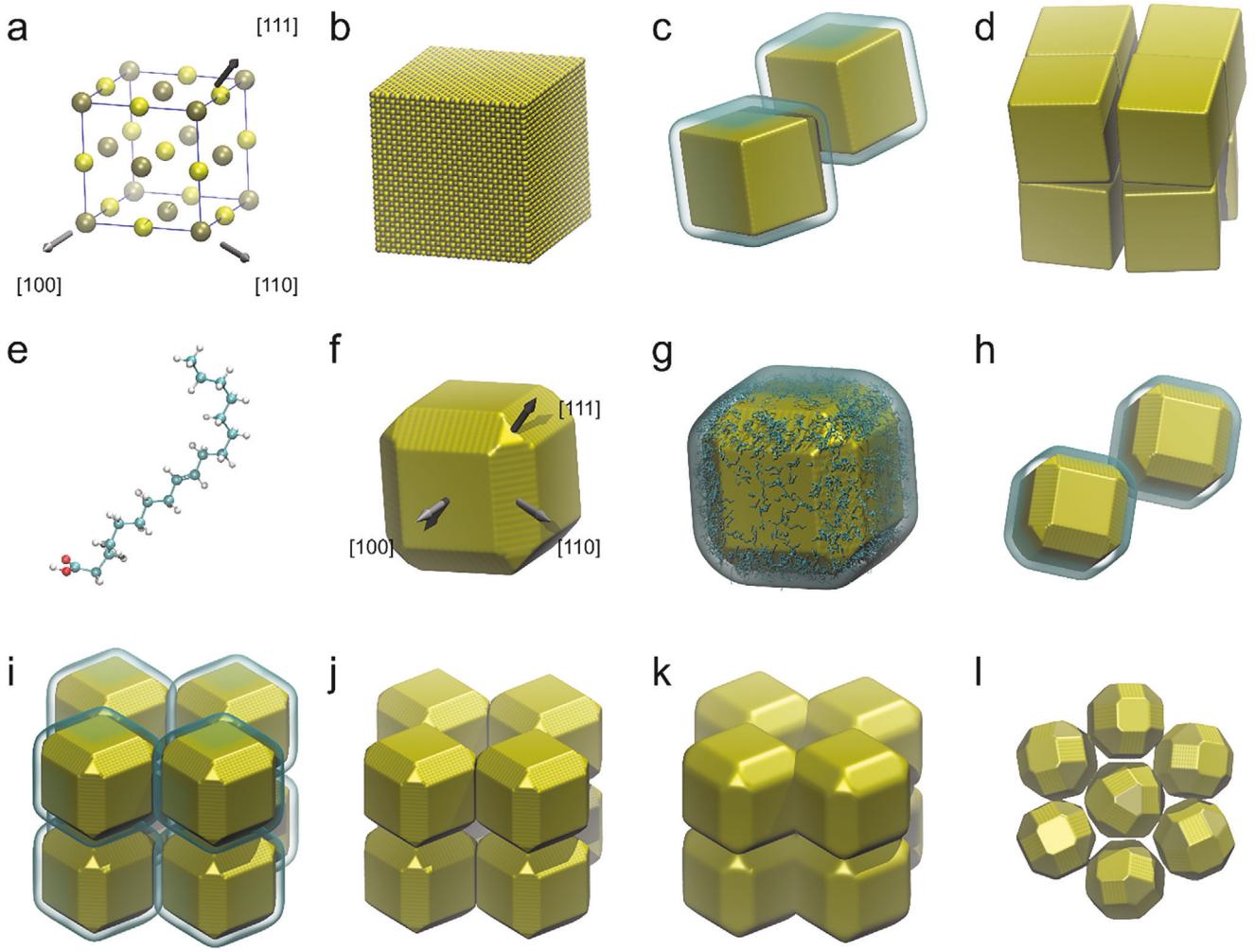

Figure 8. Crystal structure and self-assembly variants of PbSe CQDs: a) cubic unit cell of a PbSe crystalline lattice (Pb: brown, Se:yellow) with periodic box size 6.1 Å, arrows indicate the three normal axes of the three most stable crystalline planes; b) a conventional PbSe dot with the shape of the cube having the most stable {100} faces (≈10 nm in size); c) cubic colloidal dots self-assembling in dispersion; d) a resulting conventional dense cubic superlattice; e) a random conformation of a oleic acid ligand (C: cyan, O: red, H: white); f) a PbSe dot with the shape of the cube truncated to nearly spherical shape (≈10 nm in size) as the result of ligands' stronger interaction with less energetically favorable {110} and {111} faces, the arrows indicate the normal of the corresponding planes as before; g) an example of colloidal PbSe dot covered with oleic acid ligands (cyan threads, H omitted for clarity), the ligands populated randomly with probability to be attached to less stable {110} or {111} planes taken to be 3 times higher than to a more stable {100} surface (ratio chosen arbitrary, for illustrative purposes only), transparent surface indicate approximate volume occupied by QD with ligands' shell, h) illustration of two truncated dots self-assembling due to ligands' stronger interaction on edges; i–k): illustrations of organization of PbSe dots in the produced self-assembled superlattice variations, connected through truncated {110} edges, higher populated with ligands, leaving more stable {100} surfaces facing the interparticle pores until the pressure of evaporating solvent induces the layers to stack-up by {100} planes; the illustrations correspond to: i) pristine superlattice (with capping ligands), j) annealed superlattice, k) molten-salt-treated superlattice reflecting swelling and partial merging of the dots; l) illustration of a hexagonal pattern, forming possibly due to occasional growth of {111} truncated corners contributing to a more spherical shape and increasing disorder. Figure created using VMD[57] and Tachyon[58] software.

filtering at the dot interfaces.[3] In fact, Wang and co-workers demonstrated the quantum confinement effect in PbSe CQD superlattices by underpinning an increase of S from 700 to 1150 μV K^{-1} for 8.6 and 4.8 nm dots, respectively.[18]

TE characterization of thin films, especially, their thermal conductivity, is a challenging task,[20] and exploration of different probing techniques allows us to evaluate their advantages and limitations, which is rarely reported. The STPM is a contact technique where a voltage difference is applied between the stage and probe generating a temperature gradient, which allows to measurement of generated voltage and temperature at different spots over the thin film. In sharp contrast, the FDTR is a noncontact technique where a single light beam (the pump) acts as a heat source by changing the modulation frequency while a second beam (the probe), detects the resulting temperature variation through a change in the surface reflectivity.[61] Both techniques obtain thermal properties indirectly, depending on theoretical models and several properties of the films, then, subject to great variability to be considered.

STPM required a conductive substrate for accurate Seebeck coefficient measurement, as voltage difference was applied through the substrate during measurement. We chose W foil substrate due to its low resistivity (4.9 μΩ cm at 20 °C), which minimized interference with the Seebeck coefficient measurements.

For FDTR and electrical conductivity measurements, we selected SiO_2/Si substrate due to its insulating properties and well-characterized physical properties. This choice eliminated substrate contributions to electrical transport while measuring thin film electrical conductivity. Additionally, the well-modeled thermal transport properties of SiO_2/Si substrate enabled the determination of thermal conductivity in the PbSe CQD thin films.

In our experimental efforts, the thermal conductivity values κ = 3–13 W m^{-1} K^{-1} obtained by a contact STPM technique (Table 1) were quite high when compared with the values measured by a noncontact FDTR technique $\kappa \approx 0.7$ W m^{-1} K^{-1} ± 30% (Figure 6). Notably, the value obtained by FDTR is close to the theoretical limit of lattice thermal conductivity of 0.4 W m^{-1} K^{-1} for bulk PbSe.[62] At the same time, arrays of PbSe CQDs with 7.5 nm size were reported to reach even lower $\kappa \approx 0.2$ W m^{-1} K^{-1} when measured by FDTR technique,[63] mainly due to the phonon confinement and interface scattering of the CQDs.

A significant difference between the STPM and FDTR thermal conductivities observed in the current study may be due to the formation of an air and water meniscus between the tip of the STPM probe and the sample since measurements were performed under atmospheric conditions. Heat transport should occur on solid–solid (tip-sample) contact. However, heat transfer can also be influenced by air, water meniscus, or even radiation between the sample and the tip.[51,64] Shi et al. have shown that air can increase the thermal conductivity of thin films by more than one order of magnitude depending on the heated contact area between the tip and the sample.[65] Another important parameter influencing the STPM measurements is the formation of a water meniscus between the tip and the sample due to moisture since the employed temperatures were below the boiling point of water. Thermal conductance of capillary water condensation depends on the dimensions of the water meniscus, which can vary according to the surface roughness, the hydrophilic or hydrophobic nature of the surface, and the relative humidity of the air.[52] Radiation is normally ignored in the measurements near room temperature since its contribution is more significant at higher temperatures.[51] One contact parameter that can also contribute to inaccuracy in the STPM measurements is the formation of a nonconductive oxide layer on the surface of the PbSe CQD building blocks, influencing tip-sample contact.[52] It is known that the oxidation of small chalcogenide CQDs occurs quite quickly upon exposure to ambient conditions, and the oxidized surface layer could influence the electrical and thermal contacts between the STPM probe and the superlattice film, thus causing less accurate measurements.[66] Furthermore, although the STPM enables the nanometer-scale spatial resolution, this technique is sensitive to the morphologies of the specimen and the tip, hence, requiring a dedicated probe and complex heat transfer modeling to acquire consistent results.[66,67] Notably, our PbSe superlattice films feature some defects on the surface, increasing locally the surface roughness (Figure S9, Supporting Information). In fact, the STPM maps (Figure 7) show some points with drastically different κ values from the neighboring points (sometimes even negative values were measured), which could be related to surface-roughness-induced interference on the measurement. It should be stressed that the STPM measurements were carried out under basically the same atmospheric conditions and tips for the pristine, annealed, and molten-salt-treated samples, and therefore, we see the comparison between the three samples giving relative information of the treatment dependence on the thermal conductivity. Indeed, the exploitation of STPM for thin films allowed us to gain insight into 2D changes. Further investigations with different tip morphologies could help to understand the exact influence of the film roughness and air heat transfer on the absolute values of the STPM thermal conductivity measurements.[51,67,68]

Thermal and electrical properties of thin films can be influenced by surface defects and roughness. Grain boundaries and point defects at the thin film surface can introduce additional scattering centers for electron conduction leading to a higher electrical resistivity, the lattice thermal conductivity can be further reduced due to the phonon surface roughness scattering.[69] In order to minimize the effects of surface defects, the deposition of a passivation layer could uniformize the surface of the self-assembled PbSe CQD thin films and also reduce surface oxidation defects. Alumina infilling by atomic layer deposition[70] or vapor dosing with trimethylaluminum has been shown to successfully reduce defect sites, decrease surface roughness, and improve electrical conductivity.[71]

The STPM probing allowed us to demonstrate the variation of thermal conductivity, effusivity, and Seebeck coefficient between nonsuperlattice and superlattice regions within the same PbSe CQD thin films (Table 2). In pristine and molten-salt-treated films, superlattice regions were found to exhibit higher κ and effusivity in comparison with nonsuperlattice regions, while similar values of κ and effusivity were measured in superlattice/nonsuperlattice regions of the annealed film. Reduced thermal transport in randomly-ordered arrays can be related to the enhancement of different paths for interface phonon scattering.[50] Ordered structures through smaller truncated facets seem to provide fewer interfaces for phonon scattering than disordered PbSe CQDs arrays, which may present more interfaces due to the higher contact area through larger {100} facets (Figure 8i–k). It has been reported that geometry confinement is the major factor influencing the thermal conductivity of the QD superlattices.[72] Indeed higher packing density expected after oleate ligand removal by heat treatment led to lower thermal conductivity of annealed and molten-salt treated samples when compared with the pristine sample. We found that the thermal conductivity and effusivity are roughly two times more suppressed in the treated thin films than in the pristine one. The STPM data show that superlattice regions feature higher thermopower in comparison to nonsuperlattice counterparts, with an exception for a molten-salt-treated sample which shows a similar thermopower for superlattice and nonsuperlattice regions. The observed lower values of the Seebeck coefficient in randomly ordered arrays may be associated with poor contact among dots' interfaces, and accordingly, reduced carrier filtering in such non-superlattice regions.[17]

According to the modeling, the interparticle barriers play a crucial role in the transport of nanostructured material. The best fit to experimental measurements (Figure 1) is achieved if we assume that highly ordered superlattices of pristine and annealed CQDs have on average slightly shorter interparticle

distance (w_{GB} = 1.5 nm) than disordered assemblies (w_{GB} = 2.0 nm). This rather small change has, however, a significant impact on the probability of free electrons tunneling between particles, notably increasing both electric conductivity and Seebeck coefficient. CQDs' sintering during thermal annealing results in a larger area of contact, which can also be reproduced to the model by reducing interparticle pore radius (R_{pore}/R_0 = 1.0 for annealed vs 1.3 for pristine). On the other hand, treatment with molten salts produced films with higher electrical conductivity and Seebeck coefficient with only a minor difference between ordered and disordered samples. We believe that this happens due to the surface restructuring of CQDs during treatment, resulting in a large number of highly electrically conductive interparticle contacts. This correlates in our modeling with the best fit, to experimental points, achieved by assuming w_{GB} = 1.0 nm for both disordered and highly ordered molten-salt-treated samples. For the latter case, the lower height of the interparticle barrier (U_{GB} = 0.5 eV vs 5.0 eV for all other cases) suggests that a large portion of CQDs may be fused together during treatment, thus resulting in contacts similar to grain boundaries in a polycrystalline material rather than gaps between well-separated CQDs. From this point of view, it can be suggested that even a disordered molten-salt-treated sample can have electrical conductivity and Seebeck coefficient almost as high as highly ordered if it has a high enough number of such "good" contacts to form a percolating network.

Overall, when comparing the electrical and thermal transport properties of three fabricated PbSe CQD thin films, the molten-salt-assisted ligand removal affords the best-performing TE film with a calculated power factor (*PF*) of 0.217 and 0.0129 μW m^{-1} K^{-2} for superlattice and nonsuperlattice regions, respectively. The performance difference between highly-ordered and randomly-ordered closely-packed arrays of the same thin film is of one order of magnitude, which is largely influenced by the measured low electrical conductivity of nonsuperlattice region of molten-salt-treated PbSe CQD thin film. Remarkably, the superlattice region of molten-salt-treated PbSe CQD thin film demonstrated almost 100 times improvement of TE performance (*PF*) when compared with annealed PbSe CQD thin film. This improved performance was attained due to the increased electrical conductivity of molten-salt-treated PbSe CQD superlattice regions. Calculated profiles of the Seebeck coefficient and electrical conductivity as the function of chemical potential (Figure 1) revealed that all the fabricated films fall in the narrow interval close to the charge neutrality point, where the $S(\mu)$ curve makes a very steep change from *p*-type to *n*-type. This hints that the TE performance of the PbSe CQD thin films has potential for improvement as both the Seebeck coefficient and electrical conductivity can be markedly improved if *n*-type dopants are introduced.[45,73] Besides doping, another viable approach to increase the conductivity of the fabricated PbSe superlattice thin films is the conformal deposition of additional conductive material into the voids between our truncated corner-connected dots. For instance, atomic layer deposition or infiltration could be used for such conformal deposition, affording higher electrical conductivity by means of increased contact area between PbSe dots.[32,74,75]

The preparation of micrometer-thick PbSe CQD superlattice thin films over a large area is an important advancement for energy-related applications. Further development of a reproducible and scalable synthesis for PbSe CQDs is in line with large-scale fabrication demands for applications.[59,76] Superlattice structures have demonstrated emerging physical properties, which can be employed to develop thermoelectrics, photovoltaics, optoelectronics (displays, lasers, photodetectors), and catalysis.[56,59] Electrical conductivity improvements by molten-salt treatment as well as low thermal conductivity obtained by PbSe CQD ordered structures present an important step to attain thin films with enhanced properties for future technologies.[76]

4. Conclusion

We have developed a reproducible protocol affording 1-cm^2-area fabrication of 1.5-μm-thick superlattice thin films from monodisperse, phase-pure, and chemically uniform PbSe dots. The as-fabricated superlattices exhibit an uncommon self-assembling pathway into a cubic superlattice, namely, the dots are attached to the substrate by <001> planes followed by an interconnection through the {001} facets in plan-view and {110}/{111} facets in cross-sectional-view. Such 3D organization allows superlattice thin films to withstand moderate annealing or molten-salt treatments targeting insulating oleate ligand removal without significant structural and microstructural changes. Owing to the peculiar nanostructuring, pristine, annealed, and molten-salt-treated PbSe CQD thin films were found to feature structural-ordering-dependent low thermal conductivity with estimated values down to 0.7 W m^{-1} K^{-1} at room temperature. Due to the presence of the insulating capping oleate ligand on the surface of the PbSe dot building blocks, the superlattice thin films were established to exhibit low electrical conductivities, as corroborated experimentally and theoretically. Our results demonstrate that heat treatment of pristine PbSe superlattice thin films in a molten salt can boost their electrical conductivity, and accordingly, their TE performance by two orders of magnitude. Furthermore, our modeling suggests that the charge carrier concentration of all produced samples lies in the range in which both the Seebeck coefficient and electrical conductivity can be increased simultaneously by additional doping. This opens a pathway to produce materials of PbSe-based superlattices with an even higher power factor without increasing phonon contribution to thermal conductivity.

5. Experimental Section

Starting Materials: The following reagents were used as received: lead(II) acetate trihydrate ($Pb(ac)_2$•$3H_2O$, ≥99.99%, Sigma-Aldrich), selenium (Se, 100 mesh powder, ≥99.5%), trioctylphosphine (TOP, 90%, Alfa Aesar), oleic acid (OA, 90%, Sigma-Aldrich), 1-octadecene (ODE, 90%, Sigma-Aldrich), 3-(mercaptopropyl)trimethoxysilane (MPTS, 95%, Alfa Aesar), sodium hydroxide (NaOH, ≥99.0%, Supelco), cesium iodide (CsI, 99.999%, Sigma-Aldrich), lithium iodide (LiI, 99.9%, Sigma-Aldrich), and tungsten foil (W, ≥99.9%, thickness = 0.5 mm, resistivity of 4.9 μΩ cm at 20 °C, Sigma-Aldrich). TOP, CsI, LiI, and W foil were stored and handled under an inert atmosphere. Analytical reagent grade hexane (99.8%) and toluene (99.8%) were purchased from Fisher Scientific, while acetone (≥99.5%), isopropanol (≥99.8%), and ethanol (≥99.8%) were purchased from Honeywell. Ultrapure water was generated by Milli-Q Advantage A10 system (Millipore) with a resistivity of 18.2 MΩ cm.

Synthesis of Monodisperse PbSe CQDs: To prepare monodisperse PbSe CQDs, a previously reported colloidal synthesis protocol was adapted and modified to maximize the yield of monodisperse nanocrystals with the

desired shape.[16,33] First, 7.89 g of Se powder was dissolved in 100 mL of TOP while stirring overnight at 60 °C, thus generating a transparent 1 M solution of Se in TOP (Se : TOP). Next, $Pb(ac)_2 \cdot 3H_2O$ (2.8 g, 7.4 mmol), OA (6.6 g, 23.4 mmol), ODE (50 mL, 156.3 mmol) and 1 M TOP : Se solution (12 mL) were loaded into a 250 mL three-neck round-bottom flask, the flask was then connected to the Schlenk line (Chemglass), and the reaction mixture was degassed under vacuum at 130 °C for 2 h while stirring to remove any undesired low boiling liquids, such as water and acetate admixtures. The ratio between Pb and OA was kept at 1:3.2 to ensure an excess of OA for PbSe CQDs synthesis. Pb/Se ratio was defined at 1:1.6 to ensure final PbSe CQD proper stoichiometry since Se tends to evaporate ≈200 °C. Afterward, the vacuum was switched to Ar gas, and the flask was rapidly heated to 190 °C and dwelled at this temperature for 10 min. The reaction was rapidly cooled to room temperature (RT) using a water bath, and the as-synthesized PbSe CQDs were first washed by the addition of ethanol, and then by solvent mixture of hexane and isopropanol (1 : 3), while collecting both times by centrifugation at 9000 rpm for 5 min. Finally, PbSe CQDs were dispersed in 15 mL of toluene followed by centrifugation at 3000 rpm for 10 min. The supernatant with colloidal PbSe CQDs was collected and stored in the closed vial at 4 °C. The concentration of ≈30 mg mL^{-1} PbSe CQDs in toluene was obtained gravimetrically.

Preparation of the Substrates: A 500 nm-thick silicon dioxide (SiO_2) layer was grown by plasma-enhanced chemical vapor deposition on Si(100) substrate. The resultant SiO_2/Si substrate was then diced with 1 × 1 cm^2 dimensions using an automatic dicing saw. The tungsten foil used for STPM characterization where also cut with 1 × 1 cm^2 dimensions. To remove oxidation from the tungsten foil the substrates were cleaned with a 1 M NaOH solution by ultrasonication for 30 min, and after rinsed with Milli-Q water. The SiO_2/Si and tungsten foil substrates were consecutively cleaned with acetone and isopropanol by ultrasonication for 5 min and dried by N_2 flow. A MPTS and toluene 4 : 1 solution was prepared, and the substrates were dipped in the solution overnight. Prior to the self-assembling experiments, the substrates were rinsed with toluene and dried by N_2 flow.

Self-Assembling of PbSe CQDs: A dispersion of the synthesized PbSe CQDs in toluene at 10 mg mL^{-1} was prepared. A silicon substrate was placed inside a clean 5 mL glass vial to allow further place the SiO_2/Si or W foil substrate (face-up for self-assembling) with an angle of 45 °. After, 3 mL of 10 mg mL^{-1} PbSe CQDs solution was pipetted to the vial, closed by aluminum foil with three small holes for solvent evaporation. The vials were further covered with a bowl and the solvent was allowed to evaporate slowly in a time span of 20 days. Finally, self-assembled samples inside the vials were dried for 24 h in a vacuum desiccator to ensure complete solvent evaporation.

Heat Treatment Procedures: To remove residual organics (e.g., CQDs' capping ligand) and to improve their electronic properties self-assembled films were subjected to two different heat treatments: i) annealing at 400 °C for 15 min under vacuum, and then under H_2 gas flow of 100 mL min^{-1} at 400 °C for 5 min using a Thermal CVD MicroSys 400 System (Roth & Rau); ii) thermal treatment at 200 °C for 30 min under Ar gas flow of 100 mL min^{-1} in a molten salt mixture of CsI and LiI with ratio 2 : 1 inside an alumina crucible using a tubular furnace (Lenton). The molten-salt-treated films were rinsed with ultrapure water to remove salts' residuals.

Characterization: The synthesized CQDs and the self-assembled thin films were analyzed by X-ray diffraction (XRD) using X'Pert PRO (PANanalytical) diffractometer with Ni-filtered Cu K_α radiation. Scans were performed from 20 to 80° 2θ using Si zero-background sample holders. The XRD patterns were matched to the International Centre for Diffraction Data (ICDD) PDF4 database using the HighScore software package (PANalytical). The XRD data were analyzed by Le Bail fitting followed by Rietveld refinement using GSAS II software.[77]

The morphology of the films was analyzed by scanning electron microscopy (SEM) using Helios NanoLab 450S DualBeam microscopes (FEI). The focused ion beam (FIB) method was used to prepare the lamella for cross-sectional investigation. Fine microstructure and the chemical composition of the resultant PbSe CQD thin films were investigated by transmission electron microscopy (TEM), high-angle annular dark-field scanning TEM (HAADF–STEM), electron diffraction (ED), and energy-dispersive X-ray spectroscopy in STEM mode (STEM–EDX) using a probe and image aberration corrected JEM-ARM200F cold field-emission gun microscope (Jeol), operated at 200 kV and equipped with Orius SSD camera, large angle CENTURIO EDX detector, and Quantum GIF.

Infrared spectroscopy was performed to analyze organic capping ligands present on the surface of the PbSe CQD self-assembled thin films. The room temperature Fourier-transform infrared spectroscopy (FTIR) in attenuated total reflectance (ATR) mode was employed using a VERTEX 80v spectrometer (Bruker). All spectra were recorded by averaging 64 scans with a resolution of 4 cm^{-1}, and are background corrected. Spectra were recorded from 400 to 4000 cm^{-1}, with KBr beam splitter, a DLaTGS detector, and a mid-IR source.

Thermal conductivity (κ) and heat capacity (C_p) were measured by frequency domain thermoreflectance (FDTR)[61] using a 435 nm pump laser (2 mW) and a 532 nm probe laser (4 mW), respectively. To extract κ and the thermal boundary conductance (TBC) from the phase-shift curves, the most common FDTR model was used for the thin films.[78] The measurements were conducted on PbSe CQDs thin films self-assembled on SiO_2/Si substrates. An 80 nm Au thin film was deposited by sputtering on the surface to work as a reflective transducer. To reduce the number of fitting parameters, the thickness of the Au and SiO_2 layers was kept constant with the values measured by interferometry and atomic force microscopy. Initial values were taken from the literature and separated samples with 80 nm gold on Si and SiO_2/Si substrates were used to obtain independent values for Au and SiO_2 parameters. The only free parameters in the fittings are PbSe average thickness, κ, C_p, and TBC: between Au/PbSe, G_1, between PbSe/SiO_2, G_2. The best fitting was found for $G_1 = 4 \times 10^7$ GW m^{-2} K^{-1} and $G_2 = 1 \times 10^7$ GW m^{-2} K^{-1}, although, the values of G_1 and G_2 have a low influence in the final value of κ and C_p.

2D distribution of effusivity, e, and thermopower of the fabricated thin films was measured by scanning thermal probe micro-image (STPM) using an STPM-1000 (Advance Riko) under ambient atmosphere. Temperatures of the sample and thermal probe were fixed at 30 and 60 °C, respectively. The distribution mapping was obtained at a pitch of 100 µm both vertically and horizontally. Further details are described in Table S1 (Supporting Information). Thermal conductivity was calculated from $e = \sqrt{k \times \rho \times C_p}$,[79] where ρ is the density of PbSe of 8.1×10^6 g m^{-3}, and the heat capacity of PbSe was assumed to be 0.17 J g^{-1} K^{-1}.[49]

Computational Methods: Density functional theory (DFT) calculation of PbSe electronic structure was performed using the Vienna Ab initio Simulation Package (v. 6.3.1) (VASP).[80] The initial geometry of the system was selected as a primitive unit cell of *fcc* structure, the lattice parameter of which ($a = 3.1087$ Å) corresponds to the experimentally obtained crystal structure of PbSe with the lattice constant of conventional unit cell equal to 6.1213 Å at 298 K.[81] Periodic boundary conditions are used in all three directions. The projector augmented wave (PAW) method was used to describe the core electrons of Pb and Se atoms.[82] The valence electrons of both atoms and semi-core *d*-orbitals of Pb were treated using a plane wave basis set with the kinetic energy cut-off of 520 eV and spin polarization. Exchange and correlation were described using Heyd–Scuseria–Ernzerhof hybrid functional (HSE06).[83,84] Electronic structure was iteratively converged till 10^{-6} total energy difference using 8 × 8 × 8 k-points grid initiated at Γ-point. The bandgap was estimated to be 0.275 eV, in excellent agreement with other published values.[85,86] After convergence was reached, the band structure of PbSe was sampled over a 24 × 24 × 24 k – point grid using a non-self-consistent calculation including spin-orbit interaction. Band structure energies interpolated over the high symmetry lines of *fcc* lattice are shown in Figure S6, (Supporting Information).

Electronic transport coefficients were estimated within the Boltzmann transport approach as implemented in BoltzTraP2 package.[87] For this purpose, VASP band structures were interpolated onto 120 × 120 × 120 k-points grid, and the Seebeck coefficient and electric conductivity were subsequently estimated using three following approximations for electron scattering. Transport in bulk PbSe was estimated using the constant relaxation time approximation (CRTA). Using reported experimental data on electrons' and holes' mobility,[42,43] the average relaxation time was

estimated $\tau_{bulk} = 1.16 \times 10^{-13}$ s could be used for both types of charge carriers in a wide range of concentrations (Figure S2, Supporting Information). Constant mean free path approximation (CMFP) substitutes a uniform relaxation time by the ratio $\tau_{b,k} = \lambda_{free}/v_{b,k}$ evaluated for each band, b, and k-point, k, where λ_{free} is a charge carrier mean free path, assumed to be equal for all electron modes, and group velocities are directly calculated from band structure as $v_{b,k} = \delta\varepsilon_{b,k}/\hbar\delta k$. If λ_{free} is presumed to be equal to the size of the CQD (13 nm), this is the simplest approach to imitate the effect of nanostructuring. In the current study, it is used as a reference for comparison reasons. To introduce the effect of band filtering in nanostructured matter, the approach reported elsewhere was followed.[40,41,88] Within this approach, separate scattering rates are introduced for electron scattering by potential barriers at the grain boundaries, τ_{GB}, (interparticle contacts), and pores, τ_{pore}. The average relaxation time is then calculated by Matthiessen's rule, $\langle\tau\rangle^{-1} = \tau_{bulk}{}^{-1} + \tau_{GB}{}^{-1} + \tau_{pore}{}^{-1}$. The expressions for τ_{GB} and τ_{pore} can be found in the referenced papers above. The quantities necessary to estimate the scattering rates, such as carrier group velocity, $v_{b,k}$, effective mass, $m^*_{b,k}$, density-of-states, $g(\varepsilon)$, are calculated directly from the interpolated ab initial band structures, $\varepsilon_{b,k}$, leaving τ_{GB} and τ_{pore} functions of the four fitting parameters: width w_{GB} and height U_{GB} of the square "grain boundary" potential representing an interparticle contact, radius R_{pore} and height U_{pore} of a spherical potential representing a pore between adjacent particles. Lee and co-workers[88] derive R_{pore} as the maximum radius of a sphere that can be fit into a space between the four adjacent spheres in a dense packing R_0, therefore it is presumed an unambiguous function of particle size only. Furthermore, it can be useful to vary pore radius to introduce the effect of disorder and thick ligand cover, limiting the area of direct contact between CQDs. For this reason, a scaling parameter was introduced as R_{pore}/R_0 in the set. In this way defined nonuniform scattering times electronic transport, Seebeck coefficients, and electric conductivities were calculated using Boltzmann transport equations implemented in BoltzTraP2 package. Finally, effective medium approximation (EMA) corrections reported by Lee et al.[88] was applied to account for voids in CQD arrays. While, in principle, the chosen parameters (w_{GB}, U_{GB}, U_{pore}, R_{pore}/R_0) can also be estimated from rigorous calculations, their computational cost as well as the need to perform a separate study for each of the CQD treatment methods, leaves such investigation beyond the scope of the present work. Instead, it was treated as adjustable parameters and performed a grid search over parameter space to find combinations that fit experimentally measured Seebeck coefficient and electric conductivity at the same value of chemical potential, μ.

Supporting Information

Supporting Information is available from the Wiley Online Library or from the author.

Acknowledgements

The authors thank Prof. Francisco Rivadulla from Universidade de Santiago de Compostela for valuable discussion. This research was supported by Portuguese Fundação para a Ciência e a Tecnologia (FCT) through Contracts UID/Multi/04349/2020 and UI/BD/150713/2020. V.S. acknowledges support by the FCT PhD Fellowship (Grant No. SFRH/BD/143750/2019). E.M.F.V. thanks CMEMS-UMinho Strategic Projects UIDB/04436/2020 and UIDP/04436/2020. S.G and L.M thank Strategic Funding UIDB/04650/2020 and project EXPL/FIS-MAC/0947/2021. K.K. acknowledges support by the National Science Foundation grants DMR-2333388. M.G and T.M. thank JST Mirai Program grant no. JPMJMI19A1. This work is based, in part, upon research conducted under COST Action CA21101 "Confined molecular systems: from a new generation of materials to the stars" (COSY), which was supported by the European Cooperation in Science and Technology.

Conflict of Interest

The authors declare no conflict of interest.

Data Availability Statement

The data that support the findings of this study are available in the supplementary material of this article.

Keywords

self-assembling, microstructure, molten salt, seebeck coefficient, transport properties

Received: May 28, 2024
Revised: June 24, 2024
Published online: July 12, 2024

[1] A. L. Efros, L. E. Brus, *ACS Nano* **2021**, *15*, 6192.
[2] The Nobel Prize, The Nobel Prize in Chemistry **2023**, https://www.nobelprize.org/prizes/chemistry/, (accessed: November 2023).
[3] S. Yazdani, M. T. Pettes, *Nanotechnology* **2018**, *29*, 432001.
[4] M. A. Boles, M. Engel, D. V. Talapin, *Chem. Rev.* **2016**, *116*, 11220.
[5] M. Piotrowski, J. Borme, E. Carbó-Argibay, D. Sharma, N. Nicoara, S. Sadewasser, D. Y. Petrovykh, C. Rodríguez-Abreu, Y. V. Kolen'Ko, *Nanoscale Adv.* **2019**, *1*, 3049.
[6] X. Li, X. Liu, X. Liu, *Chem. Soc. Rev.* **2021**, *50*, 2074.
[7] M. Linares-Moreau, L. A. Brandner, M. d. J. Velásquez-Hernández, J. Fonseca, Y. Benseghir, J. M. Chin, D. Maspoch, C. Doonan, P. Falcaro, *Adv. Mater.* **2024**, *36*, 2309645.
[8] H. Cölfen, M. Antonietti, *Angew. Chem., Int. Ed.* **2005**, *44*, 5576.
[9] B. Ni, G. Gonzalez-Rubio, H. Cölfen, *Acc. Chem. Res.* **2022**, *55*, 1599.
[10] C. L. Bassani, G. van Anders, U. Banin, D. Baranov, Q. Chen, M. Dijkstra, M. S. Dimitriyev, E. Efrati, J. Faraudo, O. Gang, N. Gaston, R. Golestanian, G. I. Guerrero-Garcia, M. Gruenwald, A. Haji-Akbari, M. Ibáñez, M. Karg, T. Kraus, B. Lee, R. C. Van Lehn, R. J. Macfarlane, B. M. Mognetti, A. Nikoubashman, S. Osat, O. V. Prezhdo, G. M. Rotskoff, L. Saiz, A.-C. Shi, S. Skrabalak, I. I. Smalyukh, et al., *ACS Nano* **2024**, *18*, 14791.
[11] J. J. Urban, *Nat. Nanotechnol.* **2015**, *10*, 997.
[12] S. Ortega, M. Ibáñez, Y. Liu, Y. Zhang, M. V. Kovalenko, D. Cadavid, A. Cabot, *Chem. Soc. Rev.* **2017**, *46*, 3510.
[13] D. Yin, C. Dun, X. Gao, Y. Liu, X. Zhang, D. L. Carroll, M. T. Swihart, *Small* **2018**, *14*, 1801949.
[14] P. Yox, G. Viswanathan, A. Sarkar, J. Wang, K. Kovnir, In *Comprehensive Inorganic Chemistry III*, 3rd ed., Elsevier, Amsterdam **2023**, p. 45.
[15] J. Mao, Z. Liu, Z. Ren, *npj Quantum Mater.* **2016**, *1*, 16028.
[16] V. Sousa, G. Savelli, O. I. Lebedev, K. Kovnir, J. H. Correia, E. M. F. Vieira, P. Alpuim, Y. V. Kolen'ko, *Materials* **2022**, *15*, 8805.
[17] M. I. Nugraha, I. Indriyati, I. Primadona, M. Gedda, G. E. Timuda, F. Iskandar, T. D. Anthopoulos, *Adv. Mater.* **2023**, *35*, 2210683.
[18] R. Y. Wang, J. P. Feser, J. S. Lee, D. V. Talapin, R. Segalman, A. Majumdar, *Nano Lett.* **2008**, *8*, 2283.
[19] M. S. Dresselhaus, G. Chen, M. Y. Tang, R. Yang, H. Lee, D. Wang, Z. Ren, J.-P. Fleurial, P. Gogna, *Adv. Mater.* **2007**, *19*, 1043.
[20] M. Piotrowski, M. Franco, V. Sousa, J. Rodrigues, F. L. Deepak, Y. Kakefuda, N. Kawamoto, T. Baba, B. Owens-Baird, P. Alpuim, K. Kovnir, T. Mori, Y. V. Kolen'Ko, *J. Phys. Chem. C* **2018**, *122*, 27127.
[21] I. Petsagkourakis, K. Tybrandt, X. Crispin, I. Ohkubo, N. Satoh, T. Mori, *Sci. Technol. Adv. Mater.* **2018**, *19*, 836.
[22] I. Ohkubo, M. Murata, M. S. L. Lima, T. Sakurai, Y. Sugai, A. Ohi, T. Aizawa, T. Mori, *Mater. Today Energy* **2022**, *28*, 101075.
[23] R. Yanagisawa, N. Tsujii, T. Mori, P. Ruther, O. Paul, M. Nomura, *Appl. Phys. Express* **2020**, *13*, 095001.

[24] T. Zhan, R. Yamato, S. Hashimoto, M. Tomita, S. Oba, Y. Himeda, K. Mesaki, H. Takezawa, R. Yokogawa, Y. Xu, T. Matsukawa, A. Ogura, Y. Kamakura, T. Watanabe, *Sci. Technol. Adv. Mater.* **2018**, *19*, 443.
[25] J. Pinna, R. M. Koushki, D. S. Gavhane, M. Ahmadi, S. Mutalik, M. Zohaib, L. Protesescu, B. J. Kooi, G. Portale, M. A. Loi, *Adv. Mater.* **2023**, *35*, 2207364.
[26] D. M. Balazs, B. M. Matysiak, J. Momand, A. G. Shulga, M. Ibáñez, M. V. Kovalenko, B. J. Kooi, M. A. Loi, *Adv. Mater.* **2018**, *30*, 1802265.
[27] A. Abelson, C. Qian, T. Salk, Z. Luan, K. Fu, J.-G. Zheng, J. L. Wardini, M. Law, *Nat. Mater.* **2020**, *19*, 49.
[28] K. Whitham, J. Yang, B. H. Savitzky, L. F. Kourkoutis, F. Wise, T. Hanrath, *Nat. Mater.* **2016**, *15*, 557.
[29] W. J. Baumgardner, K. Whitham, T. Hanrath, *Nano Lett.* **2013**, *13*, 3225.
[30] M. M. van der Sluijs, D. Sanders, K. J. Jansen, G. Soligno, D. Vanmaekelbergh, J. L. Peters, *J. Phys. Chem. C* **2022**, *126*, 986.
[31] M. A. Boles, D. Ling, T. Hyeon, D. V. Talapin, *Nat. Mater.* **2016**, *15*, 141.
[32] C. M. Staller, S. L. Gibbs, X. Y. Gan, J. T. Bender, K. Jarvis, G. K. Ong, D. J. Milliron, *Nano Lett.* **2022**, *22*, 5009.
[33] D. Cadavid, S. Ortega, S. Illera, Y. Liu, M. Ibáñez, A. Shavel, Y. Zhang, M. Li, A. M. López, G. Noriega, O. J. Durá, M. A. López De La Torre, J. D. Prades, A. Cabot, *ACS Appl. Energy Mater.* **2020**, *3*, 2120.
[34] D. Yin, Y. Liu, C. Dun, D. L. Carroll, M. T. Swihart, *Nanoscale* **2018**, *10*, 2533.
[35] W. L. Zuo, A. Murtaza, C. Zhou, C. Kong, Y. Zhang, F. Tian, L. Wang, S. Yang, *J. Magn. Magn. Mater.* **2020**, *499*, 166250.
[36] D. V. Talapin, C. B. Murray, *Science* **2005**, *310*, 86.
[37] H. Zhang, K. Dasbiswas, N. B. Ludwig, G. Han, B. Lee, S. Vaikuntanathan, D. V. Talapin, *Nature* **2017**, *542*, 328.
[38] V. Kamysbayev, V. Srivastava, N. B. Ludwig, O. J. Borkiewicz, H. Zhang, J. Ilavsky, B. Lee, K. W. Chapman, S. Vaikuntanathan, D. V. Talapin, *ACS Nano* **2019**, *13*, 5760.
[39] Q. Gong, W. Ding, A. Bonk, H. Li, K. Wang, A. Jianu, A. Weisenburger, A. Bund, T. Bauer, *J. Power Sources* **2020**, *475*, 228674.
[40] A. Popescu, L. M. Woods, J. Martin, G. S. Nolas, *Phys. Rev. B Condens. Matter* **2009**, *79*, 205302.
[41] N. Sonnathi, A. Panwar, V. Malik, A. Bagga, *MRS Adv.* **2018**, *3*, 1329.
[42] U. Schlichting, K. H. Gobrecht, *J. Phys. Chem. Solids* **1973**, *34*, 753.
[43] C.-F. Wu, T.-R. Wei, J.-F. Li, *APL Mater.* **2016**, *4*, 104801.
[44] X. Ma, X. Shai, Y. Ding, J. Zheng, J. Wang, J. Sun, X. Li, W. Chen, T. Wei, W. Ren, L. Gao, S. Deng, C. Zeng, *Molecules* **2023**, *28*, 2629.
[45] J. Androulakis, D. Y. Chung, X. Su, L. Zhang, C. Uher, T. C. Hasapis, E. Hatzikraniotis, K. M. Paraskevopoulos, M. G. Kanatzidis, *Phys. Rev. B Condens. Matter* **2011**, *84*, 155207.
[46] C. Fang, M. A. Van Huis, D. Vanmaekelbergh, H. W. Zandbergen, *ACS Nano* **2010**, *4*, 211.
[47] A. Abelson, C. Qian, Z. Crawford, G. T. Zimanyi, M. Law, *Nano Lett.* **2022**, *22*, 9578.
[48] X. Xu, K. E. Kweon, S. Keuleyan, A. Sawvel, E. J. Cho, C. Orme, *Small* **2021**, *17*, 2101166.
[49] L. Pan, S. Mitra, L. D. Zhao, Y. Shen, Y. Wang, C. Felser, D. Berardan, *Adv. Funct. Mater.* **2016**, *26*, 5149.
[50] C. Gayner, K. K. Kar, W. Kim, *Mater. Today Energy* **2018**, *9*, 359.
[51] J. Bodzenta, A. Kaźmierczak-Bałata, K. Harris, *J. Appl. Phys.* **2020**, *127*, 031103.
[52] S. Gomès, A. Assy, P.-O. Chapuis, *Phys. Status Solidi A* **2015**, *212*, 477.
[53] S. Wang, S. Lu, X. Tian, W. Liu, Y. Si, Y. Yang, H. Qiu, H. Zhang, J. Li, *ACS Nano* **2023**, *17*, 2792.
[54] I. Coropceanu, E. M. Janke, J. Portner, D. Haubold, T. D. Nguyen, A. Das, C. P. N. Tanner, J. K. Utterback, S. W. Teitelbaum, M. H. Hudson, N. A. Sarma, A. M. Hinkle, C. J. Tassone, A. Eychmüller, D. T. Limmer, M. O. de la Cruz, N. S. Ginsberg, D. V. Talapin, *Science* **2022**, *375*, 1422.
[55] J. Liu, K. Enomoto, K. Takeda, D. Inoue, Y. J. Pu, *Chem. Sci.* **2021**, *12*, 10354.
[56] R. D. Septianto, R. Miranti, T. Kikitsu, T. Hikima, D. Hashizume, N. Matsushita, Y. Iwasa, S. Z. Bisri, *Nat. Commun.* **2023**, *14*, 2670.
[57] W. Humphrey, A. Dalke, K. Schulten, *J. Mol. Graph* **1996**, *14*, 33.
[58] J. Stone, *An Efficient Library for Parallel Ray Tracing and Animation*, University of Missouri-Rolla, Rolla **1998**.
[59] M. Micheel, R. Baruah, K. Kumar, M. Wächtler, *Adv. Mater. Interfaces* **2022**, *9*, 2201039.
[60] M. S. Kavrik, J. A. Hachtel, W. Ko, C. Qian, A. Abelson, E. B. Unlu, H. Kashyap, A. Li, J. C. Idrobo, M. Law, *Nat. Commun.* **2022**, *13*, 6802.
[61] J. Yang, C. Maragliano, A. J. Schmidt, *Rev. Sci. Instrum.* **2013**, *84*, 104904.
[62] F. Xu, D. Zhang, S. Gao, L. Yang, X. San, Z. Li, X. Qian, J. Yang, S. Wang, *Scr. Mater.* **2022**, *208*, 114360.
[63] W.-L. Ong, S. M. Rupich, D. V. Talapin, A. J. H. McGaughey, J. A. Malen, *Nat. Mater.* **2013**, *12*, 410.
[64] Y. Zhang, W. Zhu, F. Hui, M. Lanza, T. Borca-tasciuc, M. M. Rojo, *Adv. Funct. Mater.* **2020**, *30*, 1900892.
[65] L. Shi, A. Majumdar, *J. Heat Transfer* **2002**, *124*, 329.
[66] Y. Zhang, N. Kempf, M. McMurtrey, Scanning Probe Microscope to Map Thermal and Thermoelectric Properties of Combinatorial Materials, United States, **2019**.
[67] F. Gucmann, J. W. Pomeroy, M. Kuball, *Nano Today* **2021**, *39*, 101206.
[68] E. Guen, P. O. Chapuis, N. J. Kaur, P. Klapetek, S. Gomés, *Appl. Phys. Lett.* **2021**, *119*, 161602.
[69] J. Dong, A. Suwardi, X. Y. Tan, N. Jia, K. Saglik, R. Ji, X. Wang, Q. Zhu, J. Xu, Q. Yan, *Mater. Today* **2023**, *66*, 137.
[70] Y. Liu, J. Tolentino, M. Gibbs, R. Ihly, C. L. Perkins, Y. Liu, N. Crawford, J. C. Hemminger, M. Law, *Nano Lett.* **2013**, *13*, 1578.
[71] S. T. Ueda, I. Kwak, A. Abelson, S. Wolf, C. Qian, M. Law, A. C. Kummel, *Appl. Surf. Sci.* **2020**, *513*, 145812.
[72] C. Shao, J. Shiomi, *Mater. Today Phys.* **2022**, *22*, 100601.
[73] X. Wang, X. Li, Z. Zhang, C. Chen, S. Li, X. Lin, J. Sui, X. Liu, F. Cao, J. Yang, Q. Zhang, *Mater. Today Phys.* **2018**, *6*, 45.
[74] D. Lanigan, E. Thimsen, *ACS Nano* **2016**, *10*, 6744.
[75] P. Wainer, J. van Embden, E. D. Gaspera, *Adv. Mater. Interfaces* **2022**, *9*, 2201503.
[76] D. V. Talapin, M. Engel, P. V. Braun, *MRS Bull.* **2020**, *45*, 799.
[77] B. H. Toby, B. R. Von Dreele, *J. Appl. Cryst.* **2013**, *46*, 544.
[78] A. J. Schmidt, R. Cheaito, M. Chiesa, *Rev. Sci. Instrum.* **2009**, *80*, 094901.
[79] A. Jain, *Int. J. Heat Mass Transf.* **2023**, *202*, 123721.
[80] G. Kresse, J. Furthmüller, *Comput. Mater. Sci.* **1996**, *6*, 15.
[81] Y. Noda, K. Masumoto, S. Ohba, Y. Saito, K. Toriumi, Y. Iwata, I. Shibuya, *Acta. Cryst.* **1987**, *C43*, 1443.
[82] G. Kresse, D. Joubert, *Phys. Rev. B* **1999**, *59*, 1758.
[83] J. Heyd, G. E. Scuseria, M. Ernzerhof, *J. Chem. Phys.* **2003**, *118*, 8207.
[84] J. Heyd, G. E. Scuseria, M. Ernzerhof, *J. Chem. Phys.* **2006**, *124*, 219906.
[85] J. N. Zemel, J. D. Jensen, R. B. Schoolar, *Phys. Rev.* **1965**, *140*, A330.
[86] J. M. Skelton, S. C. Parker, A. Togo, I. Tanaka, A. Walsh, *Phys. Rev. B Condens. Matter* **2014**, *89*, 205203.
[87] G. K. H. Madsen, J. Carrete, M. J. Verstraete, *Comput. Phys. Commun.* **2018**, *231*, 140.
[88] H. Lee, D. Vashaee, D. Z. Wang, M. S. Dresselhaus, Z. F. Ren, G. Chen, *J. Appl. Phys.* **2010**, *107*, 094308.